



# Spatial and temporal distribution of a C-like asthenospheric component in the Rano Rahi Seamount Field, East Pacific Rise, 15°–19°S

L. S. Hall, J. J. Mahoney, and J. M. Sinton

*School of Ocean and Earth Science and Technology, University of Hawaii, Honolulu, Hawaii 96822, USA  
(lindahall@seanet.com)*

R. A. Duncan

*College of Oceanic and Atmospheric Sciences, Oregon State University, Corvallis, OR 97331, USA*

[1] Lavas of the Rano Rahi seamount field define a Nd-Pb-Sr isotopic array that connects, and substantially overlaps, the arrays of the nearby East Pacific Rise axis and 5.6–28 Ma lavas of the Pukapuka ridge system, situated between the seamount field and French Polynesia. Dating of Rano Rahi samples by <sup>40</sup>Ar-<sup>39</sup>Ar incremental heating methods yields ages between 0.23 and 4.67 Ma. Most of the dated lavas were erupted within 60 km of the axis, and no systematic isotopic variation with age is observed. The isotopic and incompatible element data indicate a persistent two-component mantle source comprising variable proportions of normal Pacific ocean-ridge-type mantle and a “C”-like Pukapuka end-member with lower  $\epsilon_{\text{Nd}}$ , higher <sup>87</sup>Sr/<sup>86</sup>Sr and <sup>206</sup>Pb/<sup>204</sup>Pb, and relative enrichment in the highly incompatible elements. The Rano Rahi data reveal peaks of low  $\epsilon_{\text{Nd}}$ , high <sup>87</sup>Sr/<sup>86</sup>Sr, and high <sup>206</sup>Pb/<sup>204</sup>Pb at about 16°–17°S and 18.5°–19°S that appear to correspond to two concentrations of C-rich mantle, probably streaming eastward from French Polynesia. The northern stream may have reached the axis more recently and/or be less continuous than the southern stream.

**Components:** 15,575 words, 14 figures, 7 tables.

**Keywords:** <sup>40</sup>Ar-<sup>39</sup>Ar geochronology; East Pacific Rise; mantle heterogeneity; mid-ocean ridge geochemistry; Rano Rahi seamounts.

**Index Terms:** 1032 Geochemistry: Mid-oceanic ridge processes (3614, 8416); 1038 Geochemistry: Mantle processes (3621); 1040 Geochemistry: Radiogenic isotope geochemistry.

**Received** 6 April 2005; **Revised** 11 November 2005; **Accepted** 6 January 2006; **Published** 28 March 2006.

Hall, L. S., J. J. Mahoney, J. M. Sinton, and R. A. Duncan (2006), Spatial and temporal distribution of a C-like asthenospheric component in the Rano Rahi Seamount Field, East Pacific Rise, 15°–19°S, *Geochem. Geophys. Geosyst.*, 7, Q03009, doi:10.1029/2005GC000994.

## 1. Introduction

[2] Dispersal of hot-spot-type mantle within the asthenosphere is poorly understood in areas far from hot spots. The East Pacific Rise between the Garrett Fracture Zone (13.4°S) and the northern boundary of the Easter Microplate (23°S; Figure 1a) provides an important case for study, because the region is distant from any active hot spots yet

the rise axis exhibits a 500-km-wide, relatively smooth peak in Nd, Pb, Sr, Ne, and He isotope ratios between 16°S and 20.7°S, culminating at about 17–17.5°S [Bach *et al.*, 1994; Mahoney *et al.*, 1994; Kurz *et al.*, 2005]. Mahoney *et al.* [1994] concluded the isotopic peak is the result of a heterogeneity embedded in the ambient asthenospheric mantle drawn into the zone of melting under the rise. They suggested that dilute hot-

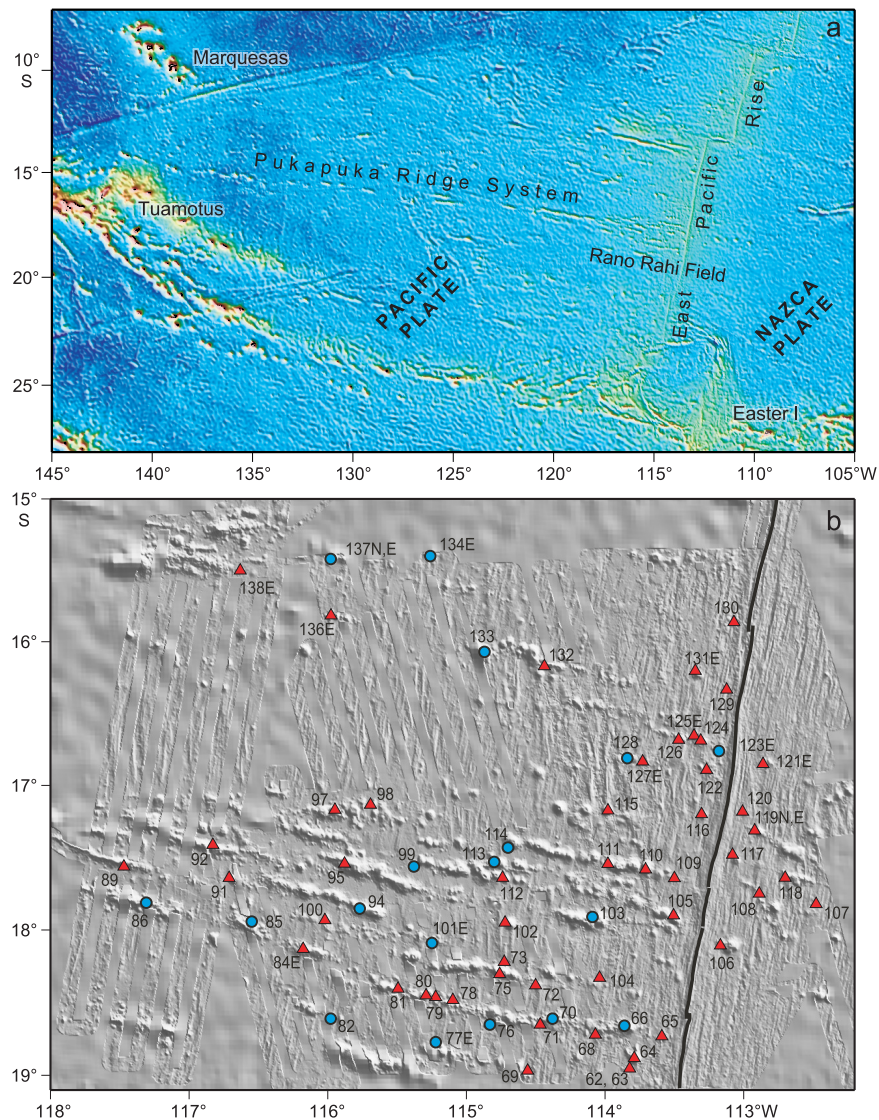


**Figure 1.** (a) Regional location map (data of *Smith and Sandwell* [1997]). (b) Map of the Rano Rahi seamount field (after *Scheirer et al.* [1996a, 1996b], including data of *Smith and Sandwell* [1997]). Black line indicates the East Pacific Rise axis. Triangles and dots mark successful dredge sites (numbered); dated samples are from sites shown with dots. Sites yielding E-MORB or both E- and N-MORB are indicated, respectively, by E and N, E; other sites yielded only N-MORB.

spot-type material was reaching the axis via long-distance lateral flow of mantle derived from a distant hot spot, such as the Marquesas to the west or Easter to the southeast. Subsequently, *Janney et al.* [2000] discovered that a very similar hot-spot-type mantle component fed the 2600-km-long Pukapuka ridge system. This system, which does not represent a hot spot trail, runs discontinuously from about 600 km west of the EPR axis to a point between the Marquesas and Tuamotu islands; ages decrease eastward along it from 28 to 5.6 Ma [*Sandwell et al.*, 1995]. The signature of the hot-spot-like isotopic component also decreases east-

ward, being smallest in the youngest Pukapuka volcanoes nearest the EPR. *Janney et al.* [2000] concluded the Pukapuka ridge system records a long-term eastward flow and dilution of this component, which they noted is similar to the proposed “C” or “common” mantle end-member of *Hanan and Graham* [1996].

[3] However, in contrast to the 500-km-wide isotopic peak at the axis, the Pukapuka ridge system at its widest is only 70 km wide. Another distinctive feature of the region, the Rano Rahi seamount field, can provide insights into post-5.6 Ma off-



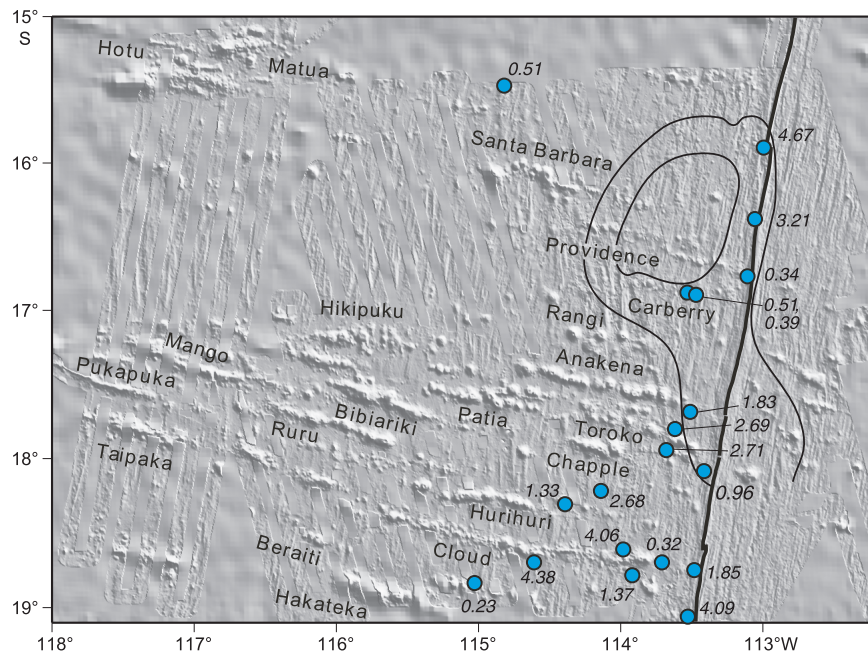


**Figure 2.** Map as in Figure 1b, except that here dots show the positions of dated lavas relative to the axis at the time of eruption; ages in Ma are indicated. Note that the dots do not represent the distribution of volcanic activity at any single time. Names of seamount chains are from *Scheirer et al.* [1996a]. Rayleigh wave phase velocities in the low-velocity “bull’s-eye” [*Forsyth et al.*, 1998] are indicated by contours at 3.70 km/s (outer contour) and 3.69 km/s (inner contour).

axis isotopic composition over a much broader zone. This field, located east of the Pukapuka Ridge system between 15°S and 19°S, is an extensive area of unusually numerous seamounts (Figure 1b), most of which lie west of the EPR axis in WNW-trending chains [*Scheirer et al.*, 1996a, 1996b]. In this paper, we present isotopic and trace element data and <sup>40</sup>Ar-<sup>39</sup>Ar age determinations for lavas of the Rano Rahi seamount field, and use the results to examine the temporal and spatial distribution of the hot-spot-like mantle component.

## 2. Previous Work, 15°–19°S EPR and Rano Rahi Seamount Field

[4] Apart from the seamount field and the axial isotopic peak, the EPR between 15°S and 19°S is unusual in several ways. The spreading rate is super-fast and asymmetric, such that the axis migrates westward [e.g., *Scheirer et al.*, 1996a]. Seafloor west of the axis subsides with age at a lower rate than average, making it shallower than normal as far as 800 km from the axis [*Cochran*, 1986]. A broad axial cross-section, together with evidence of a shallow magma chamber under about 60% of the axis between 15°S and 19°S, indicates magma supply is abundant [e.g., *Detrick et al.*,

1993; *Scheirer and Macdonald*, 1993]. A seismic low-velocity zone in the shallow mantle centered about 50 km west of the axis (Figure 2) implies that maximum melt production is skewed to the west of the axis [e.g., *Forsyth et al.*, 1998; *Forsyth and GLIMPSE Science Team*, 2004; *Dunn and Forsyth*, 2003]. Recent modeling indicates this offset may be a result of pressure-driven flow of mantle, and/or addition of hotter mantle, from the west, combined with westward migration of the axis [e.g., *Hammond and Toomey*, 2003]. Consistent with isotopic results for the axis and Pukapuka ridges, mantle tomographic data suggest that material from the southwestern Pacific may have been influencing the shallow eastern South Pacific mantle in this region for a long time [*Phipps Morgan et al.*, 1995].

[5] Interpretation of side-scan sonar data suggests the bulk of the seamounts in the Rano Rahi field may have formed within about 50 km of the axis, but reflective surfaces at greater distances imply that some relatively recent volcanic activity has occurred farther off axis [*Shen et al.*, 1993; *Scheirer et al.*, 1996a]. Like axial basalts, near-axis seamounts are the products of melting in the upwelling mantle beneath ridges, but they draw melt from a smaller volume of the melt zone; also, seamount magmas tend not to be homogenized as effectively by mixing

**Table 1.** Selected GL-08 Dredge Numbers and Positions<sup>a</sup>

Dredge	Chain	Feature	Latitude, °S	Longitude, °W	Water Depth, m	Distance From Ridge, km	Projected Latitude	Seafloor Age, Ma
<i>Pacific Plate</i>								
66	Cloud	smt	18.66	113.86	2178	44	18.75	0.6
68	Cloud	flow	18.72	114.07	3119	69	18.86	1.0
70	Cloud	smt & refl	18.61	114.38	2346	101	18.81	1.5
71	Cloud	smt & refl	18.65	114.47	3024	111	18.87	1.6
72	Hurihuri	smt & refl	18.37	114.49	1535	116	18.61	1.7
73	Hurihuri	smt	18.23	114.73	3085	144	18.52	2.1
76	Cloud	smt	18.65	114.83	3157	150	18.95	2.2
77	Hakateka	smt & refl	18.77	115.22	3301	188	19.15	2.7
78	Cloud	smt & refl	18.48	115.10	3107	180	18.85	2.6
79	Cloud	smt & refl	18.46	115.22	3061	193	18.85	2.8
80	Cloud	smt & refl	18.45	115.29	2860	203	18.86	2.9
81	Cloud	smt	18.40	115.49	1621	222	18.85	3.2
82	Beraiti	smt & refl	18.61	115.97	3333	272	19.16	3.9
85	Cloud	smt	17.94	116.55	3185	344	18.64	5.0
86	Taipaka	smt	17.81	117.31	3162	427	18.67	6.2
89	Pukapuka	smt	17.56	117.44	3245	447	18.46	6.5
91	Ruru	smt & refl	17.64	116.72	3004	364	18.38	5.3
94	Ruru	smt	17.84	115.78	2531	260	18.37	3.8
95	Bibiariki	smt	17.54	115.88	2622	280	18.11	4.1
97	Hikipuku	smt	17.17	115.95	2345	294	17.77	4.3
98	Hikipuku	smt	17.13	115.69	3266	266	17.67	3.9
99	Patia	smt & refl	17.56	115.38	3243	226	18.02	3.3
100	(S. of Ruru)	smt	17.93	116.02	2720	286	18.51	4.2
101	(S. of Ruru)	smt & refl	18.09	115.25	2877	202	18.50	2.9
102	(seamount)	smt	17.95	114.72	2485	148	18.25	2.1
103	Chapple	smt	17.91	114.10	2702	82	18.08	1.2
104	(lava flow)	flow	18.33	114.04	3076	70	18.47	1.0
105	Toroko	smt & refl	17.90	113.51	2785	23	17.95	0.3
109	Anakena	smt	17.64	113.50	2929	25	17.69	0.4
111	Anakena	smt	17.54	113.98	1832	78	17.70	1.1
112	Patia	smt	17.64	114.74	2634	155	17.95	2.2
113	Patia	smt	17.53	114.80	3022	163	17.86	2.4
114	Anakena	smt	17.44	114.71	3060	155	17.75	2.2
115	Rangi	smt	17.17	113.99	2201	89	17.35	1.3
116	(seamount)	smt & refl	17.19	113.31	2863	17	17.22	0.2
122	Carberry	smt	16.90	113.27	2896	17	16.93	0.2
123	Providence	smt	16.76	113.18	3000	12	16.78	0.2
124	Providence	smt & refl	16.70	113.31	2822	26	16.75	0.4
125	Providence	smt & refl	16.65	113.36	2925	31	16.71	0.4
126	Providence	smt & refl	16.68	113.47	2823	43	16.77	0.6
127	Carberry	smt & refl	16.83	113.73	3041	67	16.97	1.0
128	Carberry	smt & refl	16.81	113.84	2957	83	16.98	1.2
129	(near ridge)	smt	16.33	113.12	3121	10	16.35	0.2
130	(near ridge)	smt	15.96	113.07	3010	12	15.98	0.2
131	(seamount)	smt & refl	16.19	113.36	3007	37	16.27	0.5
133	Santa Barbara	smt	16.07	114.87	1622	199	16.47	2.9
134	(seamount)	smt & refl	15.40	115.26	3035	248	15.90	3.6
136	Poki	smt & refl	15.80	115.99	3147	322	16.45	4.7
137	(seamount)	smt	15.42	115.98	2350	331	16.09	4.8
138	Hotu Matua	smt & refl	15.50	116.63	3324	396	16.30	5.7
<i>Nazca Plate</i>								
106	(seamount)	smt & refl	18.11	113.17	3003	19	18.07	0.2
107	(lava flow)	smt	17.82	112.48	3030	85	17.65	1.1
108	(seamount)	smt & refl	17.79	112.89	2926	41	17.71	0.5
117	(seamount)	smt	17.48	113.09	2942	14	17.45	0.2
119	Umu	smt & refl	17.31	112.92	2971	29	17.25	0.4
120	(near ridge)	smt	17.18	113.01	2900	14	17.15	0.2
121	(seamount)	smt & refl	16.85	112.86	3003	25	16.80	0.3

as axial magmas [e.g., *Batiza and Vanko, 1984; Zindler et al., 1984; Graham et al., 1988; Niu et al., 1996, 2002*]. The only previous geochemical study of any Rano Rahi seamounts found that several near the axis at 18.2–18.9°S display a greater range of isotopic and incompatible element ratios than seen in nearby axial basalts [*Niu et al., 1996*]. Local decoupling between isotopic ratios and incompatible element ratios was documented, and argued to be a result of previous, relatively recent 1–3% partial melting of the upper mantle followed by melt migration that led to local incompatible element depletions and enrichments in the mantle. Less pronounced decoupling was observed on a regional scale along axis between 13°S and 23°S, and likewise attributed to small amounts of previous mantle melting [*Mahoney et al., 1994*]. Decoupling at both scales is consistent with melting because the more incompatible elements, such as Rb, K and Nb, are more affected than mildly incompatible elements like Ti, Y and Yb.

### 3. Sampling and Summary of Major Element Characteristics

[6] During Leg 8 of the Gloria expedition of the R/V *Melville*, we dredged samples from 70 sites within the Rano Rahi seamount field (Figure 1b; Table 1). Most dredge hauls were on the tops, flanks, or bases of seamounts, many of which were in locations showing high reflectivity on side-scan sonar records over a broad geographic area. We also recovered samples from five flat-lying reflective areas (interpreted as lava flow fields) away from any nearby seamount. In general, the mass of rock recovered and sample freshness were greater closer to the axis, but samples suitable for petrogenetic study were recovered as far as 447 km west of the axis (measured parallel to the spreading direction; Table 1). Samples selected for isotopic, trace element, and <sup>40</sup>Ar–<sup>39</sup>Ar age determinations were chosen for geographic coverage and to be representative of the range of major element compositions.

[7] Major element data (Tables A1 and A2) will be presented and discussed fully in another paper (L. S. Hall et al., *Melting beneath the Rano Rahi*

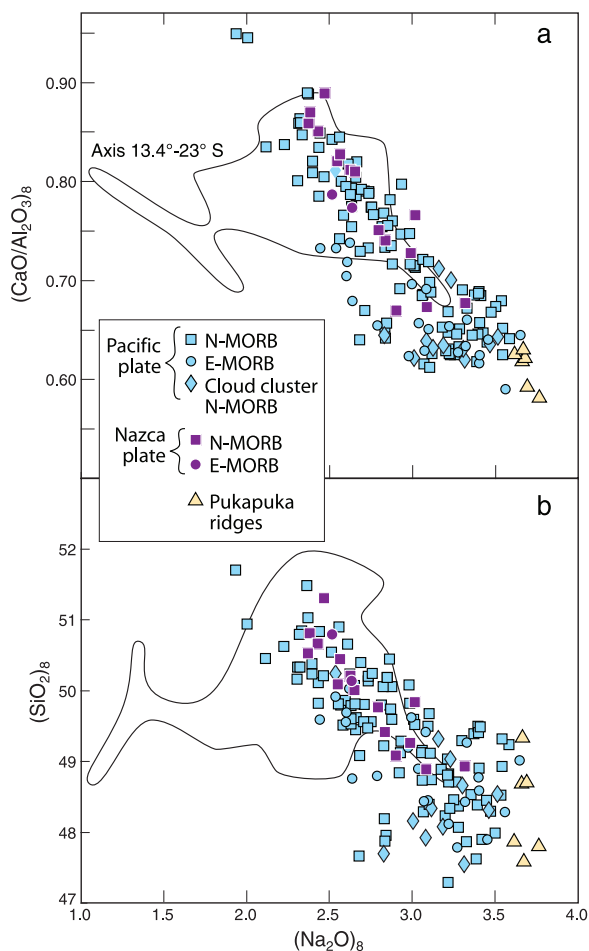


**Figure 3.**  $(\text{Na}_2\text{O})_8$  versus (a)  $(\text{CaO}/\text{Al}_2\text{O}_3)_8$  and (b)  $(\text{SiO}_2)_8$ . Solid line encloses data for axial glasses from R/V *Moana Wave* cruise MW8712 [*Sinton et al., 1991*]. Pukapuka ridge data are for samples with MgO >5.8 wt% [*Janney et al., 2000*].

seamount field, East Pacific Rise, 15–19°S, manuscript in preparation, 2006). Most of our samples are tholeiitic basalt, similar to axial MORB (mid-ocean ridge basalt) in this area [see *Sinton et al., 1991*]. The most notable differences are that the Rano Rahi samples have higher average MgO than axial basalts (8.2 wt% versus 7.1 wt%), and extend to higher  $(\text{Na}_2\text{O})_8$  and lower  $(\text{CaO}/\text{Al}_2\text{O}_3)_8$  and  $(\text{SiO}_2)_8$  values (Figure 3; the subscript-8 indicates adjustment to 8 wt% MgO by regression through the combined Rano Rahi and axial data, similar to

*Notes to Table 1:*

<sup>a</sup>Dredge numbers are for Leg 8 of the GLORIA cruise of R/V *Melville*, and include those with samples studied for isotopes and trace elements. See Figure 2 for locations of named seamount chains. Features dredged: “smt,” the slope or top of a seamount; “smt&refl,” a seamount with a patch of side-scan-reflective seafloor at its base on the map of *Scheirer et al.* [1996a]; “flow,” a flat-lying patch of reflective seafloor. Latitude, longitude, and depth are where the dredge touched bottom; dredges were usually dragged less than 1 km. Distance from the axis was measured parallel to spreading direction (azimuth 283° on the Pacific plate, 103° on the Nazca plate [*Cormier et al., 1996*]). Projected latitude is the latitude at which a line from the dredge site and parallel to the spreading direction intersects the axis. Seafloor age (sa) was calculated from  $sa = d/r$ , where d is distance from the axis and r is average accretion rate (69 km/Myr for the Pacific and 78 km/Myr for the Nazca plate [*Scheirer et al., 1996a*]).



the method of *Niu et al.* [1996]). Most of the Rano Rahi samples are compositionally normal MORB (N-MORB), although fifteen of those discussed in this paper (plus five of *Niu et al.*'s [1996]) are enriched in highly incompatible elements relative to moderately incompatible ones. These samples, with  $K_2O/TiO_2 \geq 0.10$  when measured on glass, are referred to as E-MORB below. (This E-MORB definition is roughly equivalent to the definitions of T-MORB by *Sinton et al.* [1991] and *Mahoney et al.* [1994].) Individual dredge hauls contained either N-MORB or E-MORB, with two exceptions (Figure 1b). Dredges 119 and 137 yielded both types, but the E-MORB samples are not greatly different from the associated N-MORB. For example,  $K_2O/TiO_2$  in E-MORB 119-6 and 137-1 are just 0.12 and 0.10, respectively.

#### 4. Methods

[8] The  $^{40}Ar\text{-}^{39}Ar$  age determinations were performed at Oregon State University following *Duncan and Hogan* [1994] and *Duncan* [2002]. We measured the isotopic composition of Ar in each of 4–6 temperature steps extracted by resistance-furnace heating (400°C to fusion) of ~200 mg disks cut from the freshest, most holocrystalline, aphyric interior portions of bulk rocks. Mass/charge was measured at 35, 36, 37, 38, 39 and 40 with a MAP 215/50 mass spectrometer and the data reduced with the ArArCALC software [*Koppers*, 2002]. Details are available online at <http://www.earthref.org> (on the EarthRef Digital Archive page, use keyword Rano Rahi).

[9] Isotopic and elemental analyses were performed at the University of Hawaii according to the procedures used by *Mahoney et al.* [1994] and *Neal* [2001]. For Nd, Sr, and Pb isotope measurements, acid-cleaned glass was used, except for six samples without fresh glass (see Table 2); for these, we used small chips of acid-cleaned rock. Concentrations of Nd, Sm, Sr, Rb, and Pb were determined by isotope dilution for most of the samples analyzed for isotopes. A subset of samples (mostly glasses) was analyzed for a larger suite of incompatible trace elements by inductively coupled plasma–mass spectrometry (ICP-MS). Additionally, Sr, Y, Zr, and Nb were measured for a group of bulk-rock samples by X-ray fluorescence (XRF) spectrometry. For several dredge hauls, we measured more than one sample by XRF spectrometry. We measured isotope ratios for three samples from

dredge 119. Two samples from dredge 128 were dated by  $^{40}Ar\text{-}^{39}Ar$  methods.

[10] Concentrations of Sr, Nd, and Sm measured on material from the same sample by both isotope dilution (Table 2) and ICP-MS (Table 3) agree within measurement error in all but a few cases. The elements Sr, Zr, Y, and Nb measured on glass by ICP-MS and whole rock by XRF (Table 4) from the same sample agree substantially. Small differences for a few samples are likely to reflect the presence of phenocrysts in the whole rock. For Nb concentrations <4.5 ppm, the XRF values are systematically greater by an average of 0.5 ppm. Below, we rely on measurements made on glass and use ratios of elements measured by the same method where possible.

## 5. Results

### 5.1. Ranges and Covariation of Isotope Ratios and Incompatible Elements

#### 5.1.1. Isotope Ratios

[11] The Rano Rahi lavas display a wider isotopic range than found anywhere along axis between the Garrett Fracture Zone and the Easter Microplate. The data both extend and overlap the axial data array (Figures 4 and 5); for example,  $\epsilon_{Nd} = +10.8$  to  $+6.3$  for the Rano Rahi lavas versus  $+11.1$  to  $+8.8$  along axis,  $^{87}Sr/^{86}Sr = 0.70244\text{--}0.70313$  versus  $0.70237\text{--}0.70271$ , and  $^{206}Pb/^{204}Pb = 18.078\text{--}19.280$  versus  $18.057\text{--}18.645$ . Correlations among the Rano Rahi data are slightly weaker than for the axial basalts, particularly in plots involving  $^{87}Sr/^{86}Sr$  (mostly because of several bulk-rock samples; see below). Rano Rahi isotope ratios also overlap considerably with data for the Pukapuka ridges, and the combined data for axis, seamount field, and Pukapuka ridges define a single, essentially linear array in Nd-Pb-Sr isotope space.

[12] In addition to seamount lavas, we measured isotope ratios (and trace elements) in two basalts from lava fields in flat-lying areas far from a seamount (samples 68-4 and 104-3). These lavas show no systematic isotopic differences from the seamount samples.

[13] Isotope ratios for the Rano Rahi E-MORB tend to lie toward the high- $^{87}Sr/^{86}Sr$ , high- $^{206}Pb/^{204}Pb$ , low- $\epsilon_{Nd}$  end of the Rano Rahi range, although ratios for the N-MORB overlap all but one E-MORB value. Relative to the mean data

**Table 2.** Isotope Ratios and Trace Element Concentrations by Isotope Dilution<sup>a</sup>

Sample	<sup>206</sup> Pb/ <sup>204</sup> Pb	<sup>207</sup> Pb/ <sup>204</sup> Pb	<sup>208</sup> Pb/ <sup>204</sup> Pb	<sup>87</sup> Sr/ <sup>86</sup> Sr	<sup>143</sup> Nd/ <sup>144</sup> Nd	ε <sub>Nd</sub>	Rb	Sr	Nd	Sm	Pb
66-3	18.555	15.484	38.027	0.70263	0.513109	9.1		157.4	9.550		0.383
68-4	18.488	15.498	38.007	0.70256	0.513133	9.6					0.443
<i>70-1</i>				0.70277	0.513042	7.8	0.310	161.5	6.581		
<i>71-1</i>	18.953	15.533	38.525	0.70290	0.513005	7.1	0.364	148.9	8.330	3.001	0.354
<i>73-4</i>	18.865	15.545	38.465	0.70281	0.513041	7.8	0.041	192.7	8.443	2.871	0.403
<i>76-1</i>	18.632	15.510	38.160	0.70270	0.513071	8.4		177.3	17.17	5.668	0.692
<b>77-1</b>	18.808	15.533	38.386	0.70266	0.513076	8.5	7.42	236.9	18.14	4.924	0.892
<i>78-1</i>	18.608	15.518	38.158	0.70281	0.513055	8.1	0.131	157.5	7.081	2.454	0.279
<i>79-1</i>	18.763	15.540	38.351	0.70294	0.513053	8.1					0.227
<i>80-1</i>	18.681	15.527	38.196	0.70282	0.513066	8.3	1.17	233.0	9.575	3.105	0.419
<u>81-2A</u>	18.837	15.553	38.457	0.70297	0.513024	7.5	2.05	149.3	6.010	2.117	0.234
<i>82-2</i>				0.70281	0.513040	7.8	0.269	161.2	7.976	2.726	
<i>82-2dup</i>	18.746	15.530	38.327	0.70284	0.513034	7.7					0.309
<u>85-1</u>	18.550	15.511	38.057	0.70282	0.513112	9.2	0.961	188.6	10.38	3.498	0.419
<u>86-1</u>	18.697	15.540	38.251	0.70264	0.513081	8.6	0.651	227.7	10.08		0.513
89-1	18.585	15.518	38.132	0.70257	0.513114	9.2	0.883	175.7	13.14	4.233	0.543
91-1	18.632	15.511	38.143	0.70258	0.513110	9.2	0.248	114.8	7.767	2.910	0.270
94-2	18.778	15.518	38.257	0.70262	0.513090	8.8	0.197	103.2	6.497	2.433	0.206
<u>98-1</u>	18.727	15.509	38.226	0.70284	0.513098	8.9	0.635	113.4	8.622	3.197	0.270
<u>99-3</u>	18.355	15.489	37.842	0.70246	0.513148	9.9	0.825	217.5	11.36	3.556	
100-1	18.399	15.477	37.853	0.70246	0.513140	9.8					0.395
<b>101-7</b>	18.789	15.531	38.356	0.70266	0.513093	8.8	7.01	273.4	20.65	5.831	1.175
103-3				0.70268	0.513128	9.5	0.341	104.7	7.869		
<i>104-3</i>				0.70297	0.513052	8.0	0.096	100.4	4.894	1.927	
106-1	18.919	15.524	38.395	0.70271	0.513075	8.5	0.128	107.8	6.588		0.216
107-1	18.911	15.530	38.443	0.70270	0.513058	8.2	0.482	146.1	6.459	2.413	0.243
108-4	18.850	15.539	38.377	0.70267	0.513060	8.2	0.121	124.4	6.320	2.376	0.255
109-1	18.278	15.457	37.767	0.70256	0.513189	10.7					0.124
<u>111-6</u>	18.501	15.484	37.955	0.70271	0.513134	9.6	0.718	120.9	7.495		0.263
<u>113-1</u>	18.078	15.410	37.545	0.70244	0.513163	10.2	0.179	200.6	7.479	2.493	0.303
113-1dup	18.078	15.411	37.550								
114-1				0.70268	0.513096	8.9	0.153	111.6	7.000		
116-1	18.599	15.512	38.135	0.70267	0.513131	9.6		81.6	6.454	2.632	0.226
119-1	18.710	15.503	38.185	0.70265	0.513104	9.1					0.299
119-3	18.494	15.489	37.986	0.70264	0.513111	9.2					0.393
<b>119-6</b>	18.575	15.492	38.065	0.70261	0.513110	9.2	1.00	189.9	9.583	2.767	0.344
<b>121-2</b>	18.601	15.502	38.104	0.70267	0.513107	9.1	0.963	140.6	7.790	2.706	0.305
<b>125-2</b>				0.70259	0.513141	9.8	2.90	181.6	13.23	3.984	
<b>125-2dup</b>	18.596	15.505	38.148	0.70262	0.513144	9.8	2.86	182.2	13.21	4.052	0.681
126-2	18.809	15.520	38.384	0.70298	0.513025	7.5					0.166
<b>127-1</b>	18.636	15.506	38.196	0.70271	0.513124	9.4	3.81	138.1	16.03	5.270	0.691
128-1	18.495	15.491	37.980	0.70263	0.513130	9.6	0.431	145.7	10.79	3.664	0.370
130-3	18.130	15.424	37.581	0.70247	0.513192	10.8					0.630
<b>131-3</b>	18.730	15.528	38.289	0.70257	0.513145	9.9					0.826
133-3	18.340	15.480	37.842	0.70253	0.513167	10.3	0.237	106.7	6.196	2.361	0.228
<b>134-5</b>	18.788	15.545	38.391	0.70272	0.513066	8.3	5.54	224.9	18.73	5.431	
<b>136-1</b>	18.850	15.551	38.454	0.70283	0.513077	8.5					1.361
<b>137-1</b>	18.343	15.482	37.804	0.70285	0.513159	10.1	2.86	181.0	11.84	3.827	0.455
<b>138-2</b>	19.280	15.609	38.970	0.70313	0.512965	6.3	18.3	367.1	37.97		1.947

<sup>a</sup> Sample numbers have the form dredge # - rock #; boldface indicates E-MORB, italics indicate the Cloud cluster (see text), and underlines indicate those samples for which bulk rock rather than glass was analyzed. Measurements on duplicate dissolutions and hand-picks of sample are labeled "dup." Fractionation corrections are 0.1194 for <sup>86</sup>Sr/<sup>88</sup>Sr and 0.242436 for <sup>148</sup>NdO/<sup>144</sup>NdO. Isotope ratios are reported relative to the measured value of <sup>87</sup>Sr/<sup>86</sup>Sr = 0.71024 for NBS 987 Sr, to <sup>143</sup>Nd/<sup>144</sup>Nd = 0.511850 for La Jolla Nd (0.511845, measured), and the Pb isotope values of *Todt et al.* [1996] for NBS 981 Pb. The total range measured for NBS 987 Sr over a 2-year period was ±0.00002; for La Jolla Nd it was ±0.000011 (±0.2 ε<sub>Nd</sub> units); for NBS 981 Pb it was ±0.011 for <sup>206</sup>Pb/<sup>204</sup>Pb and <sup>207</sup>Pb/<sup>204</sup>Pb, and ±0.031 for <sup>208</sup>Pb/<sup>204</sup>Pb. Within-run 2σ errors for the data reported are less than the external uncertainties on these standards. Measurements were made on a VG Sector multicollector instrument in static mode for Pb and dynamic mode for Sr and Nd. ε<sub>Nd</sub> = 0 corresponds to <sup>143</sup>Nd/<sup>144</sup>Nd = 0.51264. Total procedural blanks were 4–32 pg for Pb, <60 pg for Sr, and <10 pg for Nd. Element concentrations are in ppm. Relative uncertainties (2σ) for Rb, Sr, Nd, Sm, and Pb abundances are ~1%, <0.5%, <0.2%, <0.2%, and <1%, respectively.

**Table 3.** Trace Element Concentrations Determined by ICP-MS<sup>a</sup>

	Sr	Y	Zr	Nb	Ba	La	Ce	Pr	Nd	Sm	Eu	Gd	Tb	Dy	Ho	Er	Tm	Yb	Lu	Hf	Ta	Th	U	
73-4	193	31	98.9	0.56	0.42	2.71	9.35	1.67	8.49	2.81	1.09	3.69	0.72	4.66	1.03	2.93	0.45	3.17	0.50	2.18	0.063	0.031	0.017	
76-1	170	47	177	3.29	9.57	5.64	18.3	3.30	16.5	5.28	1.72	6.36	1.15	7.35	1.60	4.32	0.67	4.52	0.70	4.03	0.23	0.17	0.075	
77-1	229	39	185	15.2	70.1	11.7	28.1	4.12	18.1	4.89	1.64	5.80	0.99	6.19	1.34	3.62	0.53	3.72	0.58	4.03	0.97	0.86	0.32	
79-1	136	26	63.0	0.77	1.74	1.69	5.96	1.13	6.01	2.17	0.87	3.04	0.59	3.90	0.88	2.37	0.37	2.52	0.38	1.58	0.062	0.040	0.018	
80-1	23	98.6	0.60	3.78	2.89	10.3	1.80	9.48	9.41	3.10	1.24	3.98	0.72	4.61	0.95	2.78	0.39	2.82	0.38	2.35			0.025	
87-24	20	61.8	0.54	2.39	1.69	6.22	1.13	6.30	6.30	2.27	0.94	2.80	0.54	3.56	0.75	2.13	0.37	2.29	0.33	1.47			0.036	
82-2	161	27	84.0	0.93	2.57	2.30	8.18	1.53	7.87	2.63	1.02	3.30	0.61	4.04	0.90	2.51	0.38	2.63	0.42	1.99	0.074	0.049	0.023	
85-1	27	113	1.99	8.10	3.40	11.4	1.92	10.9	3.87	1.40	4.64	0.77	5.51	1.07	2.92	0.41	3.02	0.39	2.76			0.059		
89-1	176	37	140	3.26	9.05	4.88	15.0	2.68	13.5	4.27	1.48	5.12	0.91	5.74	1.28	3.34	0.49	3.44	0.54	3.24	0.24	0.16	0.071	
91-1	115	30	78.3	1.01	2.41	2.09	7.35	1.48	7.97	2.93	1.08	3.71	0.71	4.60	1.01	2.71	0.40	2.80	0.43	2.11	0.095	0.047	0.024	
98-1	29	80.3	0.86	4.33	2.19	7.52	1.41	8.21	3.31	3.31	1.31	4.56	0.79	5.75	1.28	3.50	0.47	3.32	0.45	2.08			0.039	
99-3	215	28	112	1.21	2.74	3.23	11.4	2.15	10.8	3.44	1.26	4.01	0.73	4.67	0.98	2.62	0.40	2.67	0.40	2.65	0.10	0.065	0.041	
106-1	109	27	66.0	0.75	1.36	1.73	6.17	1.21	6.66	2.44	0.97	3.27	0.63	4.09	0.92	2.49	0.37	2.54	0.38	1.72	0.063	0.032	0.018	
109-1	65	22	39.9	0.33	0.62	0.88	3.50	0.77	4.45	1.83	0.73	2.51	0.50	3.39	0.76	2.08	0.32	2.20	0.34	1.20	0.027	0.014	0.007	
111-6	26	70.0	0.78	2.77	1.87	1.87	6.61	1.31	7.71	2.94	1.15	3.90	0.74	4.95	1.05	2.97	0.39	2.88	0.39	1.84			0.039	
113-1	196	23	81.2	1.12	1.92	2.65	8.52	1.50	7.42	2.42	0.96	3.05	0.57	3.61	0.81	2.18	0.33	2.23	0.34	1.77	0.091	0.049	0.030	
116-1	82	30	63.3	0.86	1.56	1.69	5.90	1.16	6.41	2.59	0.97	3.59	0.69	4.62	1.02	2.86	0.44	2.99	0.45	1.76	0.087	0.039	0.031	
119-6	170	24	81.2	3.41	9.75	3.44	9.97	1.68	8.37	2.7	1.04	3.31	0.58	3.76	0.78	2.14	0.32	2.21	0.33	1.97	0.24	0.13	0.064	
121-2	142	24	75.4	2.72	9.44	2.92	8.82	1.55	7.82	2.63	0.96	3.27	0.59	3.82	0.80	2.20	0.33	2.21	0.34	1.83	0.18	0.12	0.050	
125-2	183	34	139	5.57	26.2	5.87	16.9	2.77	13.1	4.02	1.36	4.76	0.84	5.25	1.13	3.05	0.45	3.12	0.48	3.06	0.36	0.28	0.12	
126-2	102	30	56.9	0.67	1.70	1.46	5.16	1.03	6.00	2.37	0.92	3.25	0.64	4.47	1.02	2.88	0.44	3.10	0.49	1.60	0.073	0.031	0.009	
127-1	139	52	164	7.86	33.6	6.79	19.3	3.25	16.1	5.32	1.72	6.91	1.23	8.11	1.78	4.90	0.72	5.12	0.77	4.22	0.50	0.38	0.15	
128-1	144	35	110	1.84	4.18	3.26	10.9	2.03	10.5	3.55	1.28	4.54	0.84	5.37	1.16	3.18	0.48	3.29	0.52	2.74	0.15	0.077	0.038	
130-3	121	58	184	4.42	15.4	5.79	18.5	3.35	17.4	5.96	1.89	7.39	1.38	8.85	1.94	5.36	0.81	5.60	0.87	4.54	0.32	0.22	0.087	
131-3	212	33	151	7.21	39.4	6.97	19.3	3.14	14.4	4.15	1.43	4.83	0.84	5.21	1.13	3.03	0.46	3.04	0.47	3.26	0.49	0.37	0.14	
133-3	109	24	57.3	0.81	2.61	1.51	5.35	1.09	6.07	2.39	0.91	3.09	0.59	3.73	0.81	2.25	0.33	2.30	0.35	1.65	0.072	0.034	0.018	
134-5	224	41	186	13.7	59.9	11.3	28.0	4.29	19.8	5.63	1.92	6.69	1.11	6.74	1.43	3.72	0.53	3.69	0.56	4.33	0.89	0.83	0.30	
136-1	300	39	214	28.8	139	19.7	41.2	5.41	21.6	5.29	1.69	6.37	1.00	6.08	1.29	3.46	0.53	3.52	0.56	4.58	1.8	1.9	0.64	
138-2	365	51	360	40.8	177	29.5	65.3	8.91	37.5	9.04	2.88	10.4	1.52	8.66	1.72	4.39	0.62	4.10	0.62	7.69	2.5	2.7	0.91	
<b>BHVO-1</b>																								
meas.	394	27	176	18.8	134	15.7	38.4	5.72	24.8	6.14	2.05	6.35	0.95	5.20	0.96	2.4	0.32	2.02	0.29	4.39	1.2	1.1	0.42	
rec.	403	27.6	179	19	139	15.8	39	5.7	25.2	6.2	2.06	6.4	0.96	5.2	0.99	2.4	0.33	2.02	0.291	4.38	1.23	1.233	0.42	

<sup>a</sup> Sample numbers underlined, in boldface, or in italics as in Table 2. Concentrations are in ppm. Measurements were made with a VG PQ-2S instrument. Within-run relative standard deviations are  $\pm 2-6\%$  ( $\sigma$ ) for most elements and  $\pm 13-20\%$  for Ta, Th, and U. Recommended (rec.) values for rock standard BHVO-1 are from Govindaraju [1994]; measured (meas.) values are averages for BHVO-1 analyzed as an unknown with each batch of samples ( $n = 8$ ).



**Table 4.** Whole Rock Trace Element Concentrations by XRF<sup>a</sup>

Sample	Sr	Y	Zr	Nb
66-3	159	29	103	3.8
68-3	108	30	68	1.0
70-2	177	24	83	1.6
71-1	145	30	89	1.7
72-2	147	25	77	1.1
72-7	110	27	63	0.9
73-4	181	28	97	0.7
76-1	180	47	185	4.1
<b>77-1</b>		37	188	15.2
78-2	175	26	84	1.1
79-2	131	24	65	1.3
80-1	223	26	108	1.0
81-2A	139	21	66	1.1
82-2	152	24	80	1.2
85-1	212	32	128	2.8
94-4	83	21	51	1.3
95-1	176	19	59	0.8
97-2	111	31	72	1.0
98-1	109	33	92	1.8
99-1	227	29	119	1.4
100-1	263	26	102	1.7
<b>101-1</b>	251	35	186	14.4
<b>101-7</b>	276	41	223	12.9
102-3	160	26	93	0.9
104-1	99	30	53	0.6
105-1	133	24	71	
106-1	117	21	55	1.0
107-1	122	25	67	1.9
108-4	125	22	63	0.7
109-1	63	22	41	0.6
111-6	120	29	77	1.3
112-4	67	24	44	0.8
113-1	196	23	84	1.5
114-1	114	28	73	1.4
115-1	112	21	52	1.0
116-1	82	29	64	1.3
117-6	108	21	52	1.2
119-1	153	25	71	1.6
119-3	178	24	87	2.5
<b>119-6</b>	167	24	84	4.0
120-1	79	24	49	0.8
<b>121-2</b>	138	23	77	3.2
122-2	116	49	154	4.7
<b>123-1</b>	128	41	126	5.8
<b>123-2</b>	160	43	167	8.2
124-8	100	20	49	0.9
<b>125-2</b>	177	32	137	5.4
126-2	86	26	51	
<b>127-1</b>	133	50	164	7.7
128-1	143	34	113	2.2
129-1	99	40	108	2.4
130-3	116	57	182	4.5
130-4	131	30	89	3.1
133-3	120	28	67	1.2
<b>134-5</b>	228	40	186	13.3
<b>137-1</b>	176	33	125	4.2
137-6	127	29	82	2.0
137-8	124	28	79	1.7
<b>138-1</b>	360	48	354	40.9

**Table 4.** (continued)

Sample	Sr	Y	Zr	Nb
<b>BCR-1</b>				
meas.	328	38	193	12.3
rec.	330	38	190	14

<sup>a</sup>Sample numbers in boldface or italics as in Table 2. Concentrations are in ppm. An estimate of accuracy is provided by comparison of measured ( $n = 11$ ) and recommended [Govindaraju, 1994] values for standard BCR-1. Typical reproducibility ( $2\sigma$ ) for Sr, Y, Zr, and Nb is  $\pm 2$ , 1, 5, and 0.6 ppm, respectively. Measurements were made with a Siemens 303-AS instrument.

trend, a subset of N-MORB have slightly lower  $^{206}\text{Pb}/^{204}\text{Pb}$  (by  $\sim 0.1$ – $0.2$ ) for their  $^{87}\text{Sr}/^{86}\text{Sr}$  and  $\epsilon_{\text{Nd}}$  (Figure 5, diamonds). These N-MORB also have higher  $^{87}\text{Sr}/^{86}\text{Sr}$  and lower  $\epsilon_{\text{Nd}}$  than found for most of the Rano Rahi and axial N-MORB. This distinctive group (denoted by italics in Tables 2–5) comes from a cluster of sites in the Cloud, Beraiti, and Hurihuri chains in the southern part of the seamount field; we refer to these lavas as the Cloud cluster. Only one of our samples (126-2) from outside the Cloud cluster has similar characteristics.

### 5.1.2. Alteration Effects

[14] Three whole rock samples (137-1, 85-1, and 98-1) have notably high  $^{87}\text{Sr}/^{86}\text{Sr}$  relative to their  $\epsilon_{\text{Nd}}$  values, and a fourth (111-6) has slightly elevated  $^{87}\text{Sr}/^{86}\text{Sr}$  (Figures 4a and 5a). These samples are visibly altered, and their  $^{87}\text{Sr}/^{86}\text{Sr}$  values have probably been increased by seawater alteration. The  $^{87}\text{Sr}/^{86}\text{Sr}$  values of two other whole rock samples (80-1 and 81-2A) do not appear to be elevated appreciably.

[15] Seawater alteration also appears to have increased the concentrations of Rb, Ba, and U in all six whole rock samples. Ratios of these elements to alteration-resistant elements (e.g., Rb/La, U/Nb), when plotted relative to a ratio of two alteration-resistant elements such as Nb/Zr, are higher in the whole rock samples than in the glasses (Figure 6a). Concentrations of Rb have been affected the most. In the discussion that follows, we do not depend on  $^{87}\text{Sr}/^{86}\text{Sr}$ , Rb, Ba, or U for the whole rock samples, and in figures following Figure 6 have excluded data for these elements for these samples.

### 5.1.3. Incompatible Element Characteristics

[16] Concentrations of highly incompatible elements range widely (e.g., Nb, 0.3–41 ppm). Moderately incompatible elements have smaller but still

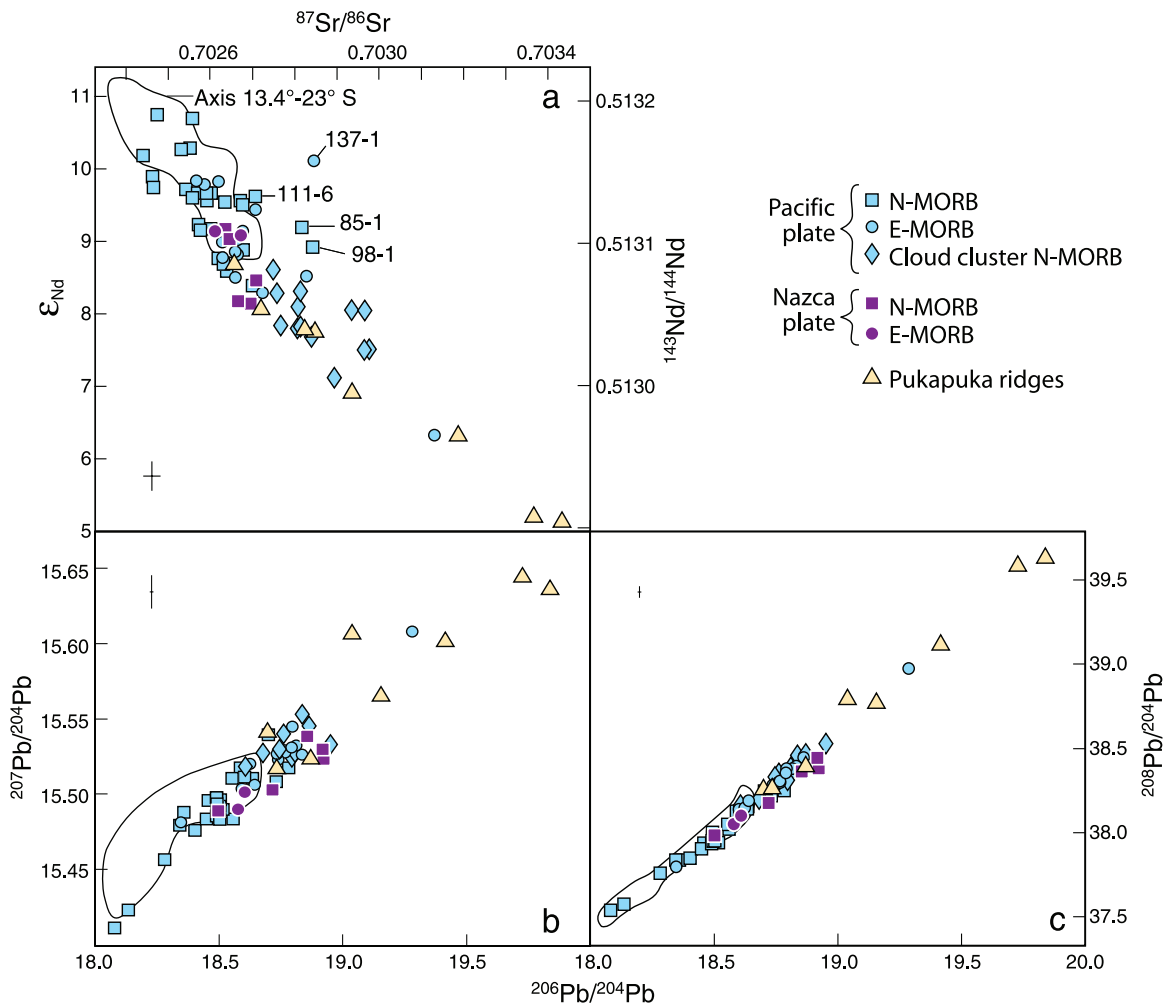


**Figure 4.** (a)  $^{87}\text{Sr}/^{86}\text{Sr}$  versus  $\epsilon_{\text{Nd}}$ , (b)  $^{207}\text{Pb}/^{204}\text{Pb}$  versus  $^{206}\text{Pb}/^{204}\text{Pb}$ , and (c)  $^{208}\text{Pb}/^{204}\text{Pb}$  versus  $^{206}\text{Pb}/^{204}\text{Pb}$ . Pukapuka ridge data are *Janney et al.*'s [2000]. Principal data sources for the 13.4–23°S EPR axis (outlined field) are *Mahoney et al.* [1994], *Bach et al.* [1994], and *Niu et al.* [1996]. Labeled data points in Figure 4a indicate bulk-rock samples with Sr isotope ratios that appear to have been elevated by seawater alteration. Note that data for sample 126-2 are shown with the diamond symbol for the Cloud cluster N-MORB in this and subsequent figures (see text). Error bars are for data of Table 2.

substantial ranges (e.g., Zr, 40–360 ppm). Primitive-mantle-normalized patterns for the Rano Rahi N-MORB are similar to those of axial N-MORB, with relative depletions in the highly incompatible elements (Figure 7). The E-MORB display flatter patterns, and four E-MORB show relative enrichment in the highly incompatible elements, similar to several Pukapuka ridge lavas. Ratios of elements with significantly different bulk solid-liquid distribution coefficients ( $D$ ) range from slightly lower to much higher than axial values when the more incompatible element is in the numerator (e.g., see Nb/Zr in Figure 6). Variation in ratios of highly incompatible elements with similar  $D$ , such as Rb/La and La/Ce, is also greater than seen along axis. Overall, correlations among incompatible element ratios are strong and, as with isotopic ratios, define a

single trend that includes axial, Rano Rahi, and Pukapuka ridge data.

[17] In contrast, ratios of highly incompatible to moderately incompatible elements form a branched array when plotted against isotope ratios (Figure 8). High- and low-Nb/Zr, Ce/Yb, etc. branches are defined by the Rano Rahi E-MORB (and Pukapuka ridge lavas) and N-MORB, respectively. The low- $\epsilon_{\text{Nd}}$ , high- $^{87}\text{Sr}/^{86}\text{Sr}$ , high- $^{206}\text{Pb}/^{204}\text{Pb}$  portion of the N-MORB branch is defined largely by the Cloud cluster lavas.

#### 5.1.4. Variations With Latitude

[18] N-MORB are present throughout the Rano Rahi field. E-MORB occur over most of the range of latitudes sampled (Figure 1b), but we did not

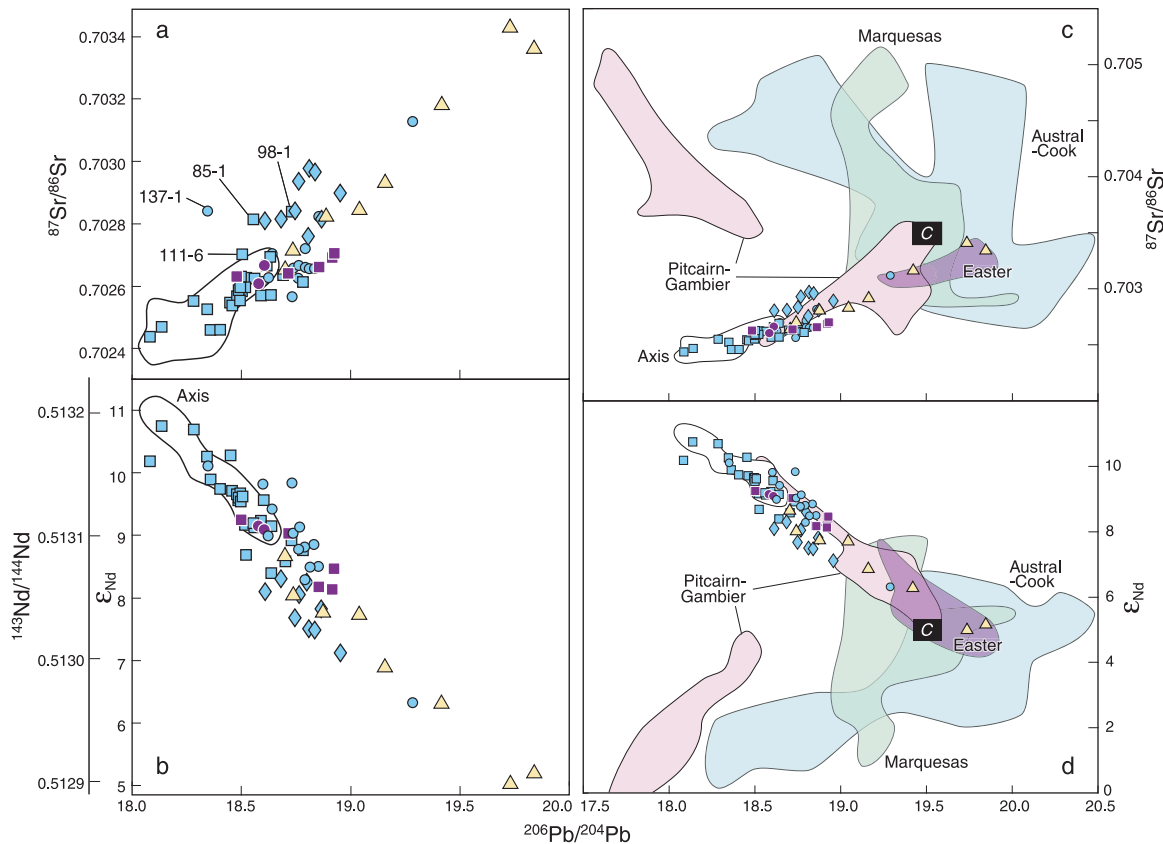


**Figure 5.** (a)  $^{87}\text{Sr}/^{86}\text{Sr}$  and (b)  $\epsilon_{\text{Nd}}$  versus  $^{206}\text{Pb}/^{204}\text{Pb}$ . Symbols and data sources are as in Figure 4. (c and d) The data relative to fields for several South Pacific island groups (island data are from GEOROC database (<http://georoc.mpch-mainz.gwdg.de>), plus J. S. Ray and J. J. Mahoney (unpublished data); a list of references is available from the first author). Composition of proposed mantle end-member C is from Hanan and Graham [1996].

find any E-MORB on either the Pacific or Nazca plates between projected latitudes (the latitude where a line through a dredge site parallel to the spreading direction intersects the axis; see Table 1 footnote) of  $17.25^\circ$  and  $18.5^\circ\text{S}$ .

[19] Isotope ratios for many Rano Rahi lavas are within or close to the values observed on the axis at their projected latitude. However, data for the Pacific-plate samples form two distinct latitudinal peaks, with maximum values in Sr and Pb isotopes and minimum values in  $\epsilon_{\text{Nd}}$ , at about  $16.3^\circ\text{S}$  and  $18.8^\circ\text{S}$  (Figures 9a–9d). These peaks, which are defined mainly by E-MORB and Cloud cluster N-MORB, do not coincide with the culmination of the broad axial isotopic peak at  $17\text{--}17.5^\circ\text{S}$ . Both Rano Rahi peaks straddle magmatic and physical segment boundaries at the axis (at  $16^\circ\text{S}$  and  $18.6^\circ\text{S}$  [Sinton *et al.*, 1991]) and thus appear to be independent of recent magmatic processes and physical segmentation at the axis.

[20] Several Pacific-plate Rano Rahi N-MORB with projected latitudes between about  $17.6^\circ\text{S}$  and  $18.8^\circ\text{S}$  have lower  $^{87}\text{Sr}/^{86}\text{Sr}$  and  $^{206}\text{Pb}/^{204}\text{Pb}$ , and higher  $\epsilon_{\text{Nd}}$ , than axial lavas in the same latitude range, approaching the regional axial “baseline” values defined by the two 250-km-long sections of axis north and south of the broad isotopic peak; that is, north of  $\sim 15.8^\circ\text{S}$  and south of  $20.7^\circ\text{S}$  (Figures 9a–9d). These two sections of the axis closely resemble each other in  $\epsilon_{\text{Nd}}$ ,  $^{87}\text{Sr}/^{86}\text{Sr}$ , and  $^{206}\text{Pb}/^{204}\text{Pb}$ . However, the section north of  $15.8^\circ\text{S}$  is characterized by lower (by  $0.02\text{--}0.04$ )  $^{207}\text{Pb}/^{204}\text{Pb}$  for a given  $^{206}\text{Pb}/^{204}\text{Pb}$  than that south of  $20.7^\circ\text{S}$ , indicating that two distinct mantle domains are present north and south of the axial isotopic peak [Mahoney *et al.*, 1994]. Three Rano Rahi lavas with high  $\epsilon_{\text{Nd}}$ , low  $^{87}\text{Sr}/^{86}\text{Sr}$ , and  $^{206}\text{Pb}/^{204}\text{Pb} < 18.3$  have low  $^{207}\text{Pb}/^{204}\text{Pb}$ , like the axial lavas north of  $15.8^\circ\text{S}$  (Figures 4b and 9d).

[21] Of the Nazca-plate samples, the four northern ones (from dredges 119 at  $17.25^\circ\text{S}$  and 121 at



**Table 5.**  $^{40}\text{Ar}$ - $^{39}\text{Ar}$  Incremental Heating Ages for Whole Rocks<sup>a</sup>

Sample GL08-	Chain or Group	Location (°S, °W)	%K	Total Fusion Age, Ma	N	Plateau Age, Ma $\pm 1\sigma$	Crustal Age, Ma	Off-Axis Origin	Position Now
<b>77-1</b>	Hakatea	18.77, 115.22	0.49	0.3	5/5	0.23 $\pm$ 0.06	2.7	173	188
				0.3	3/6	0.25 $\pm$ 0.09	2.7	171	188
82-2	Beraiti	18.61, 115.97	0.04	4.7	3/5	4.01 $\pm$ 0.46	3.9	0	272
				3.9	6/6	4.16 $\pm$ 0.37	3.9	0	272
70-1	Cloud	18.61, 114.38	0.06	2.2	5/5	1.85 $\pm$ 0.55	1.5	0	101
76-1	Cloud	18.65, 114.83	0.14	2.1	2/5	1.35 $\pm$ 0.54	2.2	57	150
				3.8	4/5	1.39 $\pm$ 0.06	2.2	54	150
78-2	Cloud	18.48, 115.10	0.05	51.8		<i>excess</i> $^{40}\text{Ar}$	2.6		180
85-2	Cloud	17.94, 116.55	0.12	7.5	3/5	4.07 $\pm$ 1.25	5.0	63	344
				5.5	3/5	4.05 $\pm$ 0.20	5.0	65	344
66-3	Cloud	18.66, 113.86	0.11	0.5	4/5	0.32 $\pm$ 0.30	0.6	22	44
				16.2		<i>excess</i> $^{40}\text{Ar}$	0.6		44
81-2A	Cloud	18.40, 115.49	0.21	43.0		<i>excess</i> $^{40}\text{Ar}$	3.2		222
86-1	Taipaka	17.81, 117.31	0.11	4.3	5/5	4.38 $\pm$ 4.47	6.2	124	427
				15.2		<i>excess</i> $^{40}\text{Ar}$	6.2		427
<b>101-7</b>	Ruru	18.09, 115.25	0.54	1.5	3/5	1.29 $\pm$ 0.15	2.9	113	202
				1.8	3/5	1.37 $\pm$ 0.05	2.9	108	202
94-4	Ruru	17.84, 115.78	0.05	3.2	5/5	2.68 $\pm$ 0.77	3.8	75	260
104-1	flow	18.33, 114.04	0.03	349.2		<i>excess</i> $^{40}\text{Ar}$	1.0		70
103-3	Chapple	17.91, 114.10	0.07	1.1	3/4	0.96 $\pm$ 0.03	1.2	16	82
99-1	Patia	17.56, 115.38	0.13	3.0	5/5	2.71 $\pm$ 0.23	3.3	39	226
113-2	Patia	17.53, 114.80	0.11	2.9	5/6	2.69 $\pm$ 0.27	2.4	0	163
105-1	seamount	17.90, 113.51	0.03	9.3		<i>excess</i> $^{40}\text{Ar}$	0.3		23
109-1	Toroko	17.64, 113.50	0.02	375.0		<i>excess</i> $^{40}\text{Ar}$	0.4		25
111-6	Anakena	17.54, 113.98	0.05	6.8		<i>excess</i> $^{40}\text{Ar}$	1.1		78
114-1	Anakena	17.44, 114.71	0.06	6.2	3/5	1.83 $\pm$ 0.48	2.2	29	155
<b>119-6</b>	Nazca	17.31, 112.92		2.5		<i>excess</i> $^{40}\text{Ar}$	0.4		29
128-1	Carberry	16.81, 113.84	0.18	0.9	4/5	0.51 $\pm$ 0.65	1.2	48	83
128-3	Carberry	16.81, 113.84	0.18	0.6	3/5	0.30 $\pm$ 0.13	1.2	63	83
				1.7	2/5	0.47 $\pm$ 0.09	1.2	51	83
<b>123-2</b>	Sta. Barbara	16.76, 113.18	0.26	2.0	5/5	0.34 $\pm$ 1.96*	0.2	0	12
133-3	Sta. Barbara	16.07, 114.87	0.14	19.3	5/5	3.21 $\pm$ 1.79*	2.9	0	199
<b>134-5</b>	H. Matua	15.40, 115.26	0.41	0.6	5/6	0.52 $\pm$ 0.04	3.6	212	248
				0.5	4/5	0.50 $\pm$ 0.09	3.6	213	248
137-2	H. Matua	15.42, 115.98	0.17	8.3	3/5	4.67 $\pm$ 0.32	4.8	8	331

<sup>a</sup> Sample numbers in boldface or italics as in Table 2. Individual step compositions and other details are at <http://www.earthref.org> (on the EarthRef Digital Archive page, use keyword Rano Rahi). Ages are reported relative to biotite monitor FCT-3 (28.04  $\pm$  0.12 Ma), which is calibrated against hornblende Mmhb-1 (523.5 Ma [Renne et al., 1994]). Plateau ages are the mean of concordant step ages (N = steps used/number of steps), weighted by the inverse of their variances. In two cases (\*) the isochron age is preferred because of evidence for small amounts of mantle-derived initial Ar. Calculations use the following decay and reactor interference constants:  $\lambda_e = 0.581 \times 10^{-10} \text{ yr}^{-1}$ ,  $\lambda_{\beta} = 4.963 \times 10^{-10} \text{ yr}^{-1}$ ;  $(^{36}\text{Ar}/^{37}\text{Ar})_{\text{Ca}} = 0.000264$ ,  $(^{39}\text{Ar}/^{37}\text{Ar})_{\text{Ca}} = 0.000673$ ,  $(^{40}\text{Ar}/^{39}\text{Ar})_{\text{Ca}} = 0.01$ . J is the neutron fluence factor, determined from measured monitor  $^{40}\text{Ar}/^{39}\text{Ar}$ . Distance at eruption = (sa - a)  $\times$  r, where sa is seafloor age, a is the sample's  $^{40}\text{Ar}$ - $^{39}\text{Ar}$  plateau age, and r is the average seafloor accretion rate (69 km/Myr).

16.80°S) have isotope ratios in or close to the axial range. Those from dredges 106–108 at 17.65–18.07°S have  $^{87}\text{Sr}/^{86}\text{Sr}$  in or slightly above the axial range at their projected latitudes, but lower  $\epsilon_{\text{Nd}}$  and higher  $^{206}\text{Pb}/^{204}\text{Pb}$  than found anywhere on axis.

[22] Ratios of highly over moderately incompatible elements, such as Rb/Nd and Nb/Zr, rise to peaks at latitudes of about 15.9–17.0°S and 18.5–19.2°S (Figures 9e and 9f), corresponding to the two isotopic peaks in our Pacific-plate samples. High values of such ratios also occur in places along the

axis, but the Rano Rahi lavas reach significantly greater values. For axial basalts in the 13–23°S region, ratios of moderately incompatible elements with broadly similar *D*, such as Pb/Nd, change little. In contrast, Pb/Nd in the Rano Rahi basalts rises to two peaks at the same latitudes as those for Rb/Nd and Nb/Zr (Figure 9g). Note that whereas the Cloud Cluster samples are important in defining the southern peak in isotope ratios, the southern peak in incompatible element ratios is largely defined by E-MORB in Figures 9e and 9f and, to a lesser extent, Figure 9g. (Note also that isotope

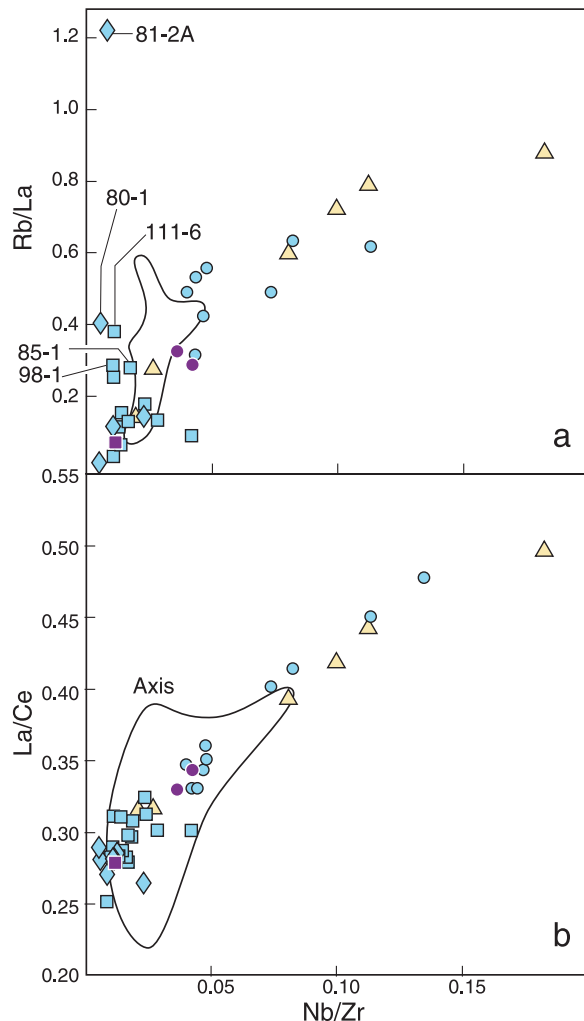


**Figure 6.** (a) Rb/La and (b) La/Ce versus Nb/Zr. Symbols are as in Figure 4. Labels in Figure 6a indicate bulk-rock samples.

data are available for several samples for which trace element data are incomplete or lacking.)

[23] Minimum values of ratios of highly incompatible elements over moderately incompatible elements, such as Rb/Nd and Nb/Zr, show modest northward increases within the seamount field, as do axial minimum values (Figures 9e and 9f). However, the minimum values for these ratios are lower, overall, than found along axis. The lowest values are near 18.5°S, near the northern boundary of the Cloud cluster.

## 5.2. Ages of Rano Rahi Lavas

[24] Nineteen samples of twenty-six analyzed yielded acceptable  $^{40}\text{Ar}$ - $^{39}\text{Ar}$  plateau or isochron ages (Table 5). These samples were dredged west

of the axis at distances between 12 and 427 km (Figure 1b). The ages vary from 0.23 to 4.67 Ma.

[25] The main impediment to obtaining reliable crystallization ages in these petrographically fresh samples is variable retention of mantle-derived  $^{40}\text{Ar}$ , often called “excess Ar.” Seven samples contained excess  $^{40}\text{Ar}$ , from which no reliable crystallization age could be determined. In samples where excess Ar was not significant, step ages formed a concordant series, comprising a majority of the gas released, from which we calculated a plateau age (mean weighted by the inverse of the variance); e.g., sample 99-1 (Figure 10a). In some cases, the highest temperature step produced an age greater than the plateau, which we interpret as a memory (line blank) effect; e.g., sample 103-3 (Figure 10b). Excess Ar is apparent in samples with variable step ages that exceed the crustal age (Figure 10c). In two instances (samples 123-2 and 133-3) excess Ar was minimal and of uniform isotopic composition, such that isochrons developed; from them we calculated crystallization ages and non-atmospheric initial Ar compositions of 299–300; e.g., sample 133-3 (Figure 10d). Seven of nine dated samples that were analyzed twice produced identical results, within analytical error, whereas excess  $^{40}\text{Ar}$  was identified in one of the pair of the remaining two samples.

[26] Because the measured range of ages is substantial, spatial geochemical variations within the Rano Rahi field do not represent a snapshot of, for example, the two-dimensional mantle or magma source variation at any single time. Distance from the axis at the time of eruption (Table 5; Figure 2) has been calculated for the dated samples using an average crustal accretion rate of 69 km/Ma for the Pacific plate in this region for the last 5 Myr [Scheirer *et al.*, 1996a]. Five samples yielded ages greater than, but within one standard deviation in analytical error of, the adjacent seafloor ages (samples 70-1, 82-2, 113-2, 123-2, and 133-3). We assign these samples a distance at eruption of 0 km. Although the seamount field extends more than 450 km from the axis, the dated basalts all erupted within 213 km of the axis. The two dated samples dredged farthest from the axis both yielded ages of less than 1 Ma; both are E-MORB: sample 77-1, with an estimated eruption distance of 172 km, and sample 134-5 at 213 km. Among dated lavas older than 1 Ma, all erupted within 125 km of the axis. Regardless of age, most of the dated lavas were erupted within 60 km of the axis, confirming suggestions from side-scan sonar

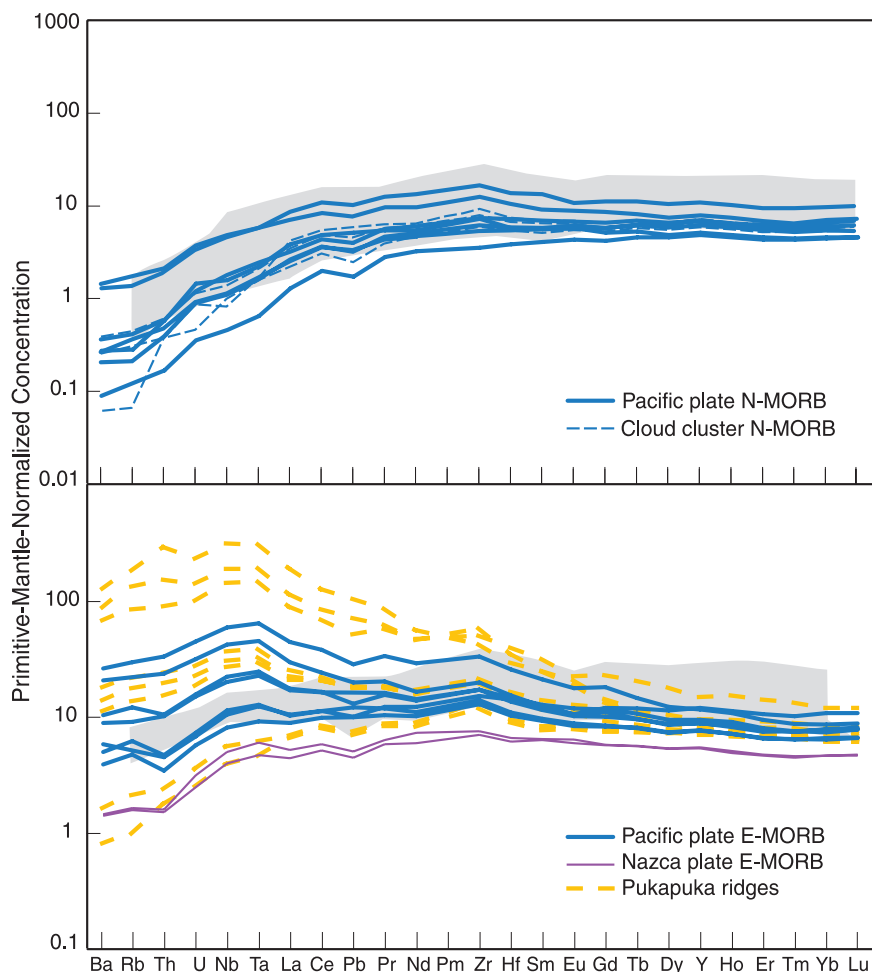


**Figure 7.** Incompatible element patterns of selected Rano Rahi (top) N-MORB and (bottom) E-MORB relative to the range for 13.4–23°S axial N- and E-MORB (gray fields, from data of *Bach et al.* [1994], *Niu et al.* [1996], and J. Sinton (unpublished data)). Pukapuka ridge data are from *Janney et al.* [2000]. Concentrations are normalized to estimated primitive-mantle values of *Sun and McDonough* [1989].

reflectivity [*Scheirer et al.*, 1996a]. The average eruption distance of the dated N-MORB is 36 km ( $\pm 36$  km,  $1\sigma$ ).

[27] No significant correlation exists between eruption age and isotope or incompatible element ratios for the dated Rano Rahi basalts (Figures 11a–11c). Likewise, no overall isotopic correlation is discernible with original distance from the axis (Figures 11d and 11e). Lavas formed within 60 km of the axis encompass nearly the entire isotopic range among the dated samples. The five erupted at distances  $\geq 75$  km show much less isotopic variation, but given their small number, it is not clear this result is meaningful. Lavas erupted at distances  $>100$  km have a narrow range of relatively high Nb/Zr, whereas lavas formed

closer to the axis, both E-MORB and N-MORB, have lower values (Figure 11f).

## 6. Discussion and Conclusions

### 6.1. Similarity of Rano Rahi Lavas to Pukapuka Ridge Lavas

[28] The collinear isotopic array defined by the axial, Rano Rahi, and Pukapuka ridge data indicates the mantle in this region consists of two principal end-members, ambient “baseline” N-MORB-source mantle and Pukapuka-type mantle. The former is best represented by the low- $^{207}\text{Pb}/^{204}\text{Pb}$  section of axis north of 15.8°S, judging from the three Rano Rahi samples with similarly low  $^{207}\text{Pb}/^{204}\text{Pb}$  (Figures 4b and 9d).



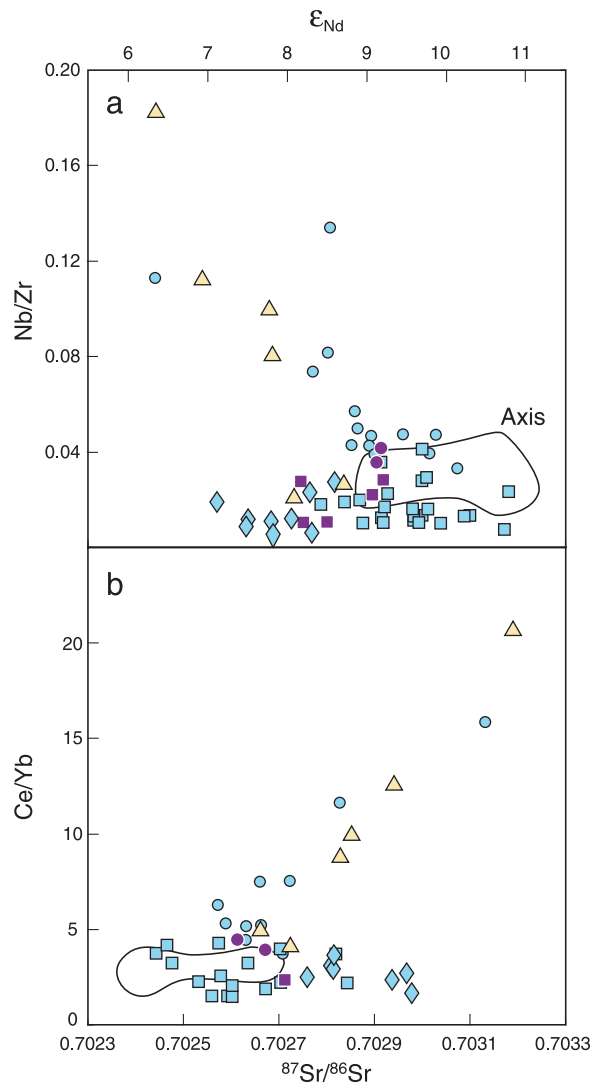


**Figure 8.** Covariation of isotope and incompatible element ratios. Symbols are as in Figure 4.

These lavas have projected latitudes between 15.98°S and 17.86°S. The northern mantle domain thus appears to extend southward well into the region of the axial isotopic peak, although its presence along axis is obscured by the abundance of basalt with higher <sup>87</sup>Sr/<sup>86</sup>Sr, higher <sup>206</sup>Pb/<sup>204</sup>Pb, and lower ε<sub>Nd</sub>. The Pukapuka end-member appears to lie rather close to the postulated C or “common” mantle component [Janney *et al.*, 2000] (Figures 5c and 5d). Isotope arrays for several South Pacific island groups also converge broadly toward this composition, including those of the Marquesas and Tuamotus, which respectively lie north and south of the western end of the Pukapuka ridge system. Hanan and Graham [1996] suggested C-type compositions represent anciently subducted, recycled oceanic lithosphere delivered to the upper

mantle by multiple plumes. Janney *et al.* [2000] proposed that a larger than usual amount of C-type mantle is present within the shallow asthenosphere in the region of the French Polynesian hot spots and is diluted with increasing distance from these hot spots, at least in the corridor covered by the Pukapuka ridges. Our results are entirely consistent with this interpretation in that they confirm the presence of significant amounts of C-type material within the MORB-source mantle east of the Pukapuka ridge system in the post-5.6 Ma period. Thus a relatively simple pattern of prolonged eastward flow of asthenosphere can explain most of the observed isotopic variation. A recent interpretation of near-axis seismic data [e.g., Hammond and Toomey, 2003] offers additional support for eastward asthenospheric flow in this region.

[29] The Rano Rahi lavas differ isotopically from the Pukapuka ridge samples as a group in having less C-like signatures. However, the three youngest, easternmost Pukapuka ridge samples are very like some of the Rano Rahi lavas in isotopic (and incompatible element) ratios. They were erupted between 7.4 and 5.6 Ma at 21–145 km from the axis (see Figure 11), whereas more C-like Pukapuka ridge magmas were formed at greater distances, beneath thicker lithosphere [Janney *et al.*, 2000]. Rano Rahi lavas with isotope ratios overlapping those of the eastern Pukapuka ridge samples represent an age range of more than 4 Myr and are found over a N-S distance of ~300 km. Thus, although not distributed uniformly, C-rich asthenosphere similar to that which fed the Pukapuka ridges has been present for a significant time over a much wider zone than the 70-km-width of the Pukapuka ridge system alone. Within our study area, an upper limit on the current width of this zone is provided by the ~500 km width of the broad axial isotopic peak. Farther afield, recent data indicate C-rich mantle in the sources of the Hotu Matua seamounts (Figure 2) and, farther north, the Sojourn and Brown ridges [Donnelly *et al.*, 2003].

## 6.2. Effects of Degree and Depth of Melting

[30] Expression of the C-type end-member is greater, overall, beneath the seamount field than along axis. The lack of curvature in the combined axial, Rano Rahi, and Pukapuka ridge isotopic array (Figures 4 and 5) implies that concentration ratios of Sr/Nd, Sr/Pb, and Nd/Pb in this end-member and the ambient N-MORB-source end-member are

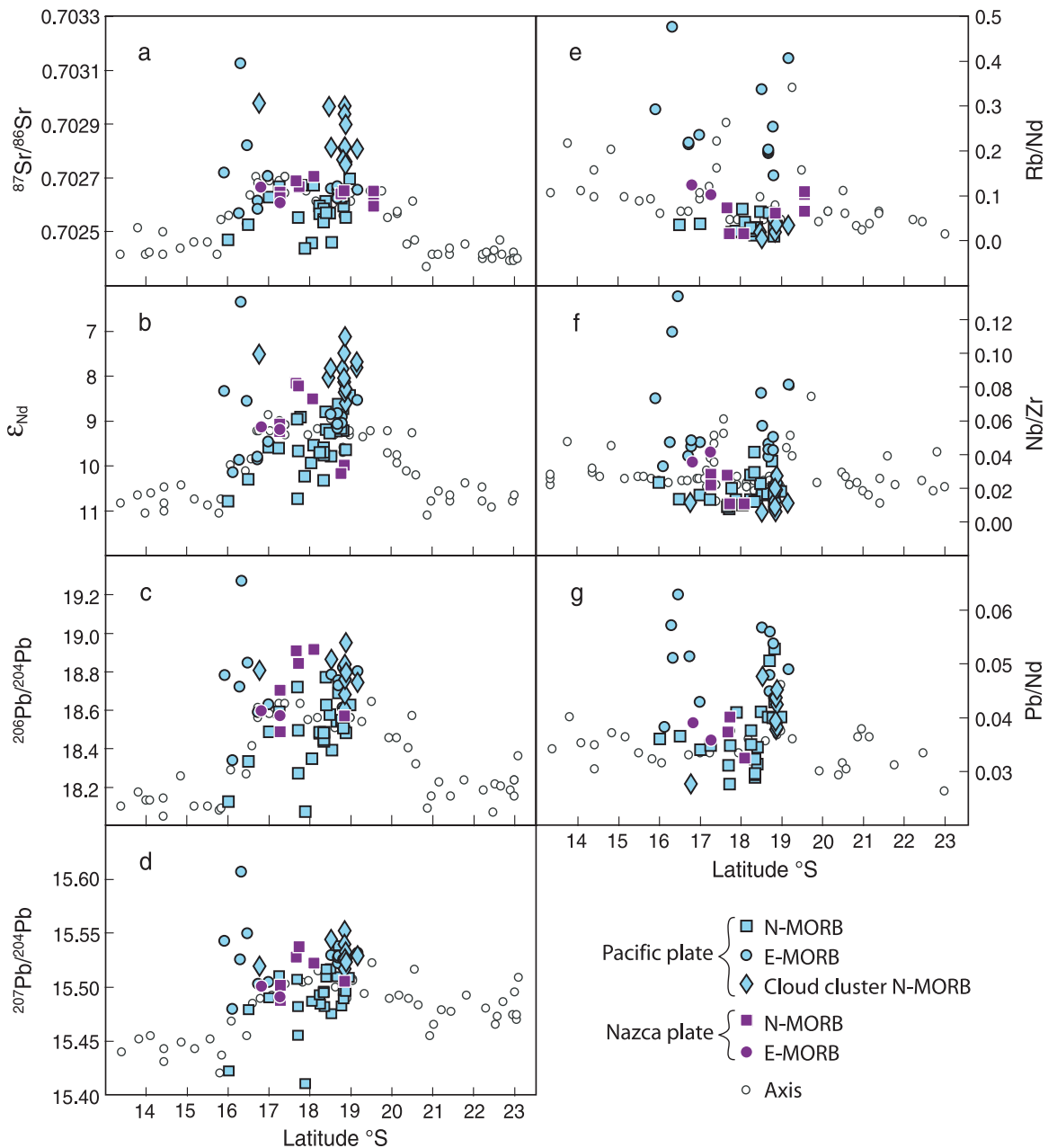


**Figure 9.** Latitudinal variation of isotope and incompatible element ratios. Data sources are as in Figure 4, plus *Macdougall and Lugmair* [1986] and *White et al.* [1987]. Rano Rahi data are at projected latitudes (see text). Note that the  $\epsilon_{\text{Nd}}$  scale is reversed.

rather similar (either in the solid state or in melts, so long as  $D$  values for Sr, Nd, and Pb are rather similar during melting). Precise estimation of the proportion of  $C$ -type material in the basalts is difficult, however, because the concentrations of these elements in the  $C$ -type mantle are poorly known, isotope ratios of this end-member are only approximately known and, in particular, a combination of mixing and differential melting of end-members appears likely (see below). Nevertheless,

consideration of simple mixing models provides useful insights. Curve A in Figure 12a schematically illustrates variable mixing of two internally homogeneous sources, assuming the  $C$ -type end-member has slightly lower  $\epsilon_{\text{Nd}}$  (+4.7) and slightly higher  $^{206}\text{Pb}/^{204}\text{Pb}$  (19.9) than the lowest- $\epsilon_{\text{Nd}}$  Pukapuka ridge lavas. These values are consistent with rough lower and upper limits of about +4.5 and 20, respectively, suggested for this end-member by companion plots of isotope ratio versus

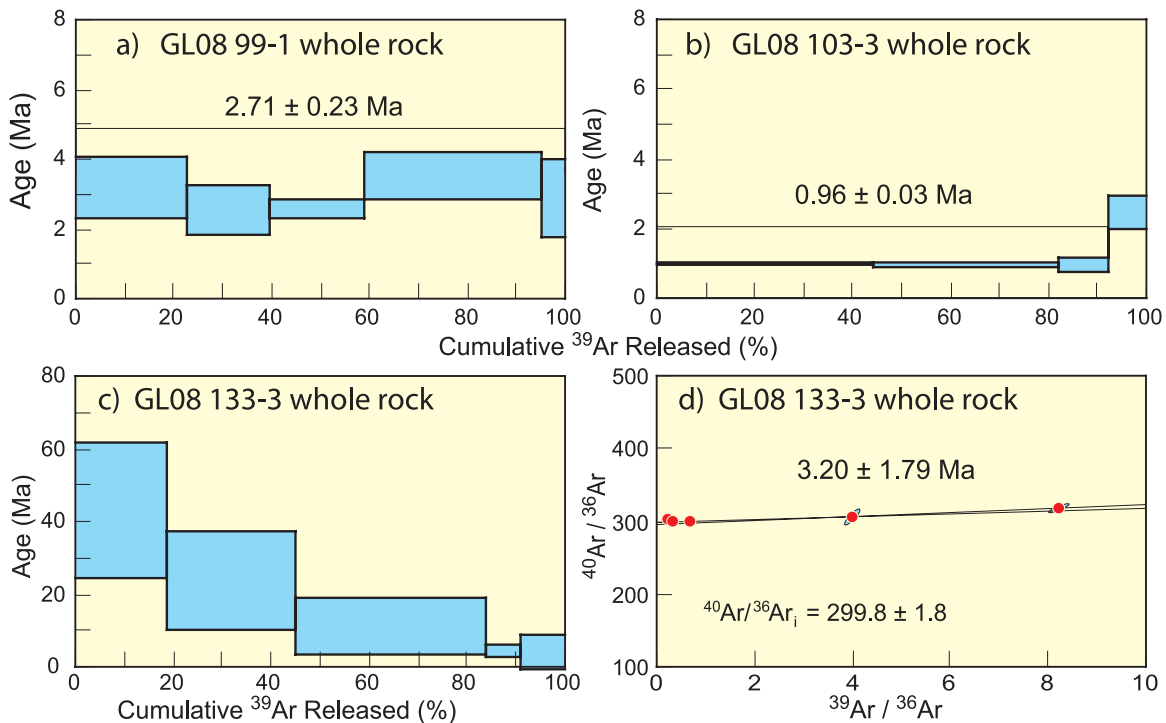


**Figure 10.** Representative age determinations from  $^{40}\text{Ar}$ - $^{39}\text{Ar}$  incremental heating experiments. (a–c) Heating step ages are plotted against cumulative gas released (temperature) in age spectra. (d) Ar-isotopic compositions from heating steps are plotted to determine an isochron age. In Figure 10a all step ages are concordant, and their weighted mean age produces a “plateau age.” In Figure 10b the highest temperature step age is discordant from the ages derived from the majority of gas released. In Figure 10c, step ages are discordant and much older than the inferred age of underlying crust because of the presence of excess (inherited)  $^{40}\text{Ar}$ . The isochron diagram for the same experiment (Figure 10d) reveals a common initial  $^{40}\text{Ar}/^{36}\text{Ar}$  exceeding the atmospheric value (295.5) and yields a crystallization age from the slope of the linear fit to the step compositions.

concentration ratios with Nd or Pb in the denominator (not shown). Curve B is also for mixing of sources, except in this case the C-type end-member is a model residue from which a 2% partial melt was previously extracted. Curve C is for mixing of a 5% partial melt of the high- $\epsilon_{\text{Nd}}$  source and a 1% melt of the C-type source of curve A. It can be seen that most of the Rano Rahi data lie within these curves.

[31] Figure 12b shows Nd isotope ratio versus Pb/Nd. The Pb/Nd ratio in basaltic systems is insensitive to crystal fractionation (unlike ratios involving Sr), and in this diagram simple mixing of homogeneous end-members should produce essentially linear arrays. The combined axial, Rano Rahi, and Pukapuka ridge data do define a rough overall correlation, but significant variation is evident in Pb/Nd at a given  $\epsilon_{\text{Nd}}$  value. Together with variable mixing of sources and intrinsic heterogeneity in the end-members, variation in amount of partial melting is indicated. Most of the E-MORB and Pukapuka ridge lavas appear to

represent lower-degree melts of their sources than most of the non-Cloud-cluster N-MORB; the Pb/Nd values of the two lowest- $\epsilon_{\text{Nd}}$  Pukapuka ridge samples (which are markedly alkalic [Janney *et al.*, 2000]) suggest very small fractions of partial melting, on the order of only 1% if taken at face value. The positions of most of the Cloud cluster lavas in Figures 12a and 12b may be explained if they are relatively low-degree melts of mixed sources in which the C-type end-member previously lost a small amount of melt. With the assumptions used in constructing Figure 12 and allowing for end-member source heterogeneity, the proportion of C-type material involved could range from roughly 30–50% for the Cloud cluster, from less than 2% to more than 20% among the other N-MORB, from roughly 60% to less than 5% among the E-MORB, and from more than 80% to less than 20% for the Pukapuka ridge lavas.

[32] Both the Pacific-plate Rano Rahi E-MORB and Cloud cluster N-MORB have low  $(\text{CaO}/\text{Al}_2\text{O}_3)_8$  and high  $(\text{Na}_2\text{O})_8$  relative to the axial



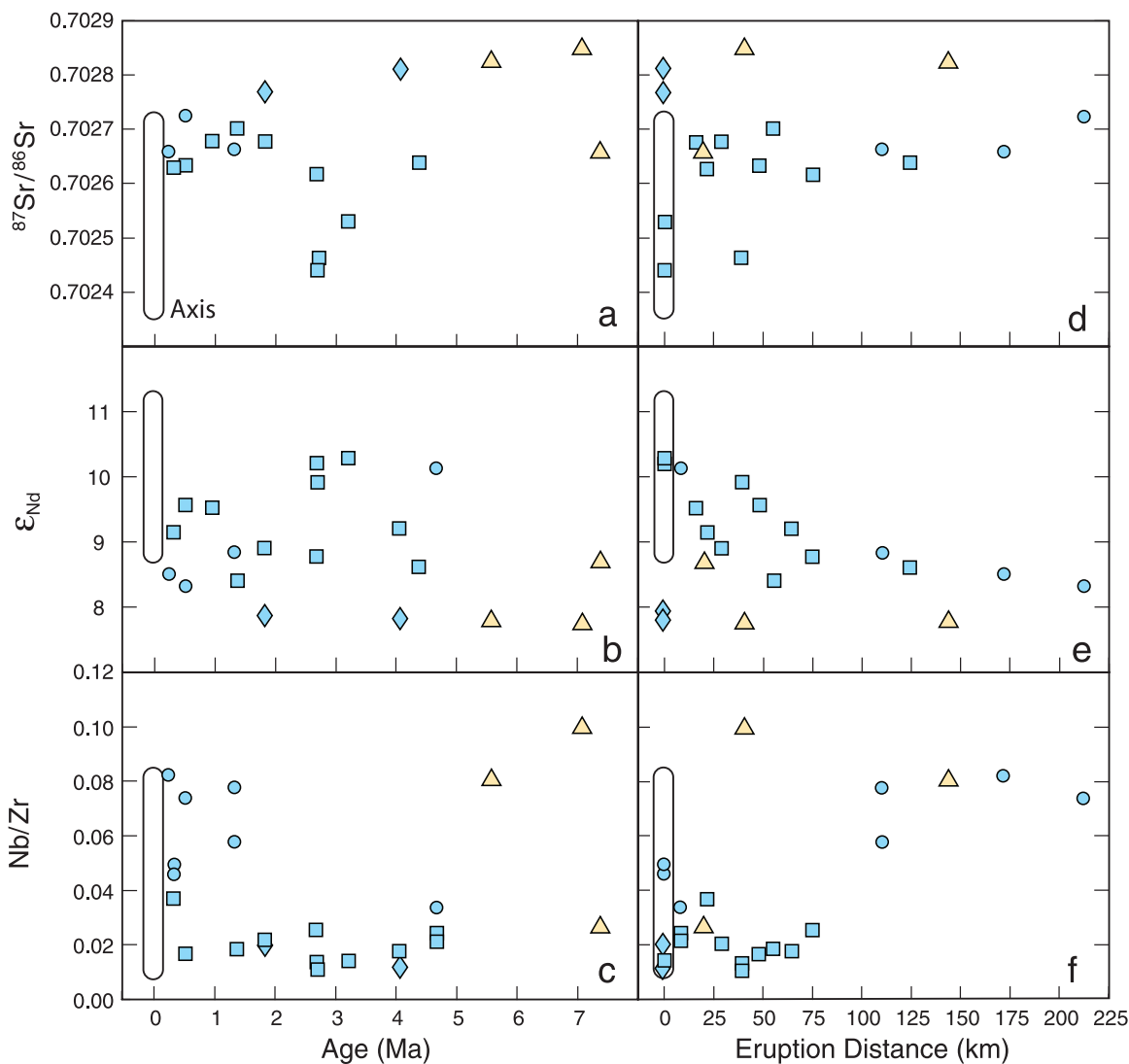


**Figure 11.** Variations versus (a–c) age and (d–f) distance from axis at eruption for the dated Rano Rahi lavas and easternmost Pukapuka ridge samples. Symbols are as in Figure 4.

basalts, approaching values for the Pukapuka ridges (Figures 3 and 13). They also have low  $(\text{SiO}_2)_8$ . Other Rano Rahi N-MORB span nearly the entire range of  $(\text{CaO}/\text{Al}_2\text{O}_3)_8$  and  $(\text{SiO}_2)_8$  for seamount field and axis combined, and some have higher  $(\text{CaO}/\text{Al}_2\text{O}_3)_8$  than found along axis. The most straightforward interpretation is that most of the E-MORB and Cloud cluster N-MORB (as well as some of the other N-MORB) were produced by lesser amounts of partial melting at somewhat greater mean depths than most axial lavas. The most C-like isotopic compositions are, with one exception (126-2), found in the low- $(\text{CaO}/\text{Al}_2\text{O}_3)_8$  E-MORB, Cloud cluster, and Pukapuka ridge samples (Figures 13a and 13b). Taken together, these results are consistent with a source in which the C-type component is unevenly distributed and

slightly more fusible, perhaps beginning to melt at greater depths [cf. *Niu et al.*, 1996].

[33] Although isotope ratios more C-like than axial values at the same projected latitude (Figure 9) are explainable in this context, several young Rano Rahi basalts have significantly higher  $\epsilon_{\text{Nd}}$  and lower Pb and Sr isotope ratios than the nearby axis. These characteristics suggest that the local volumes of mantle that melted to form these lavas simply happen to have been small enough to avoid including much of the C-type component, regardless of its physical disposition in the source (e.g., as veins, streaks, blobs).

[34] For the combined Rano Rahi E-MORB and non-Cloud-cluster N-MORB, ratios of highly incompatible to moderately incompatible elements

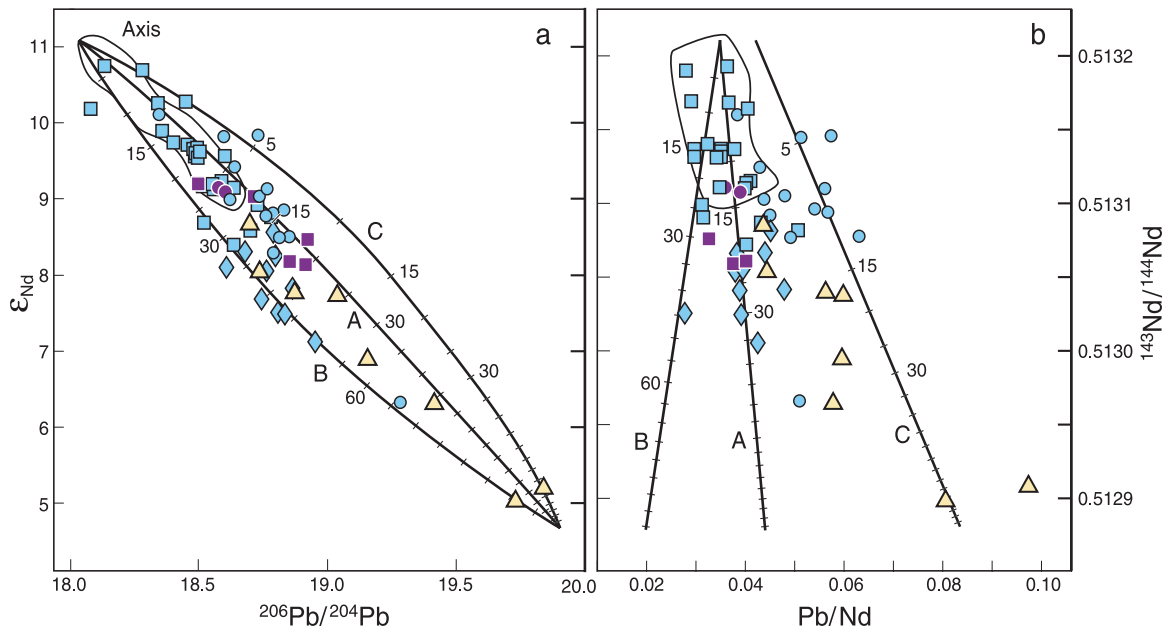


**Figure 12.** (a)  $\epsilon_{Nd}$  versus  $^{206}Pb/^{204}Pb$ . Symbols are as in Figure 4. Model mixing curves illustrate source mixing (curve A), mixing of a 5% aggregate fractional melt [Shaw, 1970] of the high- $\epsilon_{Nd}$ , ambient MORB-source end-member and a 1% melt of the C-type end-member (curve C), and source mixing in which the C-type end-member has previously lost a 2% fractional melt (curve B). (b)  $\epsilon_{Nd}$  versus Pb/Nd concentration ratio; the mixing lines correspond to the curves in Figure 12a. In both panels, tick marks indicate the proportion of material from the C-type end-member. Assumed distribution coefficients are from Workman and Hart [2005], as are the Nd and Pb concentrations of the high- $\epsilon_{Nd}$  source (0.58 ppm and 0.02 ppm, respectively). The C-type source is assumed to have the Nd concentration (1.73 ppm) of the model enriched mantle peridotite of Ito and Mahoney [2005] but one-third less Pb (0.076 ppm). End-member isotopic values used are  $\epsilon_{Nd} = +4.7$  and  $^{206}Pb/^{204}Pb = 19.90$ , and  $\epsilon_{Nd} = +11.1$  and  $^{206}Pb/^{204}Pb = 18.03$ .

such as Ce/Yb (Figure 13c) show a rough overall increase with decreasing  $(CaO/Al_2O_3)_8$ , as expected for control by partial melting, whereas such ratios remain low over the range of  $(CaO/Al_2O_3)_8$  in the Cloud cluster samples. However, ratios of moderately incompatible elements with broadly similar  $D$ , such as Pb/Nd, in the Cloud cluster are more similar to those of other low- $(CaO/Al_2O_3)_8$  lavas (Figure 13d). The Cloud cluster also exhibits decoupling between highly incompatible elements and isotope ratios (Figure 8). Similar features were documented for a dredge haul (MW52) from a near-axis seamount at 18.9°S by Niu *et al.* [1996], who concluded that an earlier episode of low-degree partial melting had partially stripped the source of the more incompatible elements before the melting episode that produced the lavas. Overall, the characteristics of the Cloud cluster are consistent with such an origin.

[35] Ratios of heavy rare earth elements provide some insight into depth of melting, because they are sensitive indicators of garnet in the source.

Melting of spinel peridotite, stable at pressures less than about 2.7 GPa ( $\sim 90$  km depth) [e.g., Herzberg *et al.*, 2000], produces a markedly different trajectory in Figure 14 than melting of garnet peridotite (or garnet pyroxenite, which, however, provides little depth resolution as it may exist at the same mantle depths as spinel peridotite). The combined axial, Rano Rahi, and Pukapuka ridge data form an array that lies much closer to a melt path for pure spinel peridotite than to one for pure garnet peridotite. Most of the data are encompassed by the model curves for 1–15% of partial melting, and nearly all are consistent with less than a 40% contribution from melting in the presence of garnet. A contribution of  $\sim 60$ –70% is suggested for three Pukapuka ridge lavas [cf. Janney *et al.*, 2000] and one Rano Rahi E-MORB (138-2). However, this is likely to be an upper limit for these four samples because they are also the ones with the most C-like isotope ratios (the curves shown are for a model source containing 25% of C-type mantle; assumption of a greater proportion of this end-member in the sources of these samples lowers the estimated amount of melt derived from garnet

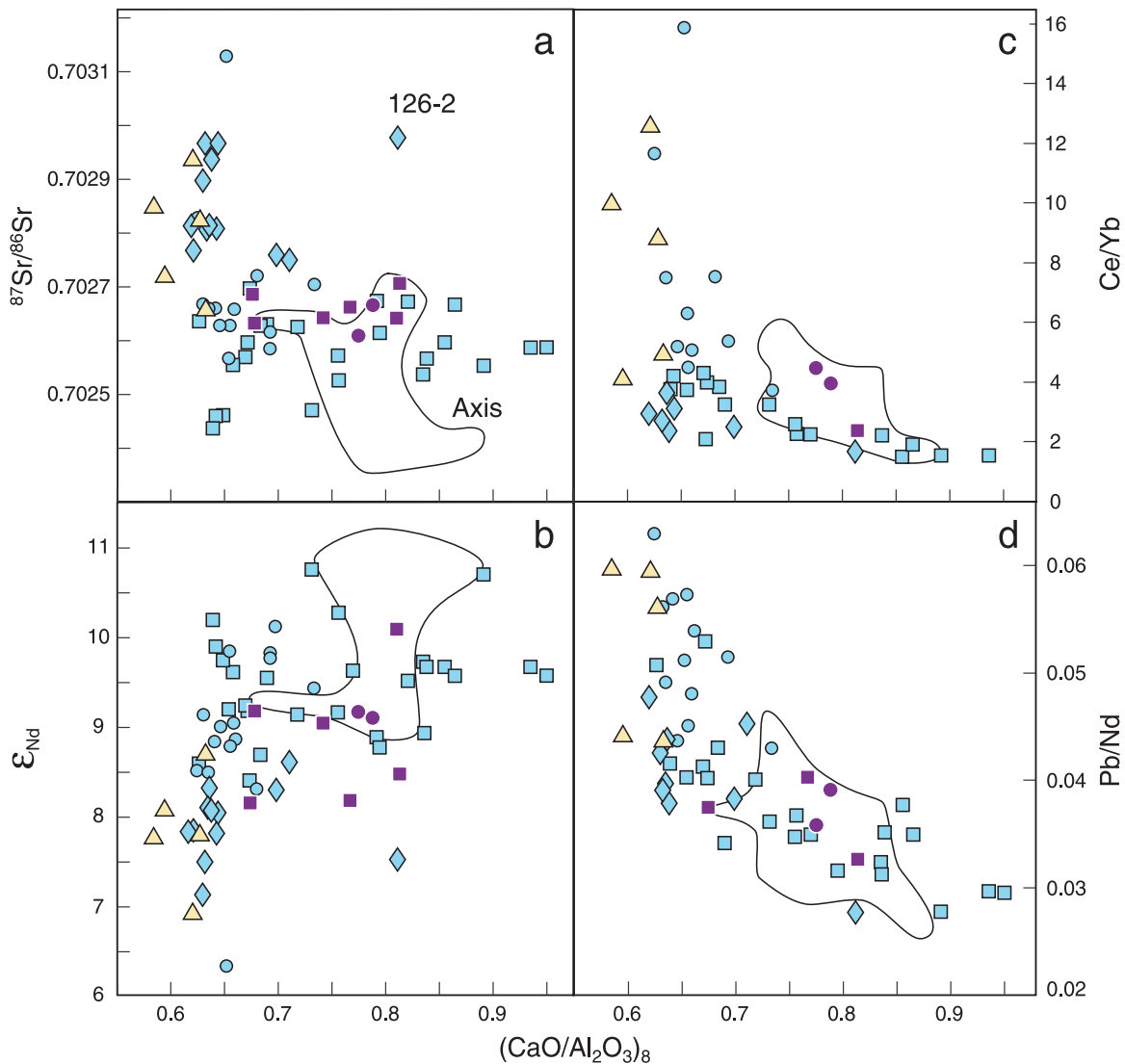


**Figure 13.**  $(\text{CaO}/\text{Al}_2\text{O}_3)_8$  versus isotope and incompatible element ratios. Symbols are as in Figure 4.

peridotite). The positions of the curves in Figure 14 also can vary with a different choice of melting model, distribution coefficients, end-member compositions, and/or mineral proportions. However, the conclusion that melting occurred predominantly in spinel facies mantle is difficult to avoid. In contrast, we caution that because no single mixture of end-members applies to all the lavas, the figure provides only a rough idea of the amount of partial melting. For example, from the curves shown, 10–15% of partial melting would be estimated for most of the Cloud cluster lavas; however, values of 4–9% are suggested if a 2% fractional melt is assumed to have been removed previously from the *C*-type end-member in the garnet stability field.

[36] Several of the Cloud cluster data points lie slightly below curve B in Figure 12a. This could be

a result of end-member heterogeneity or because actual distribution coefficients, amount of previous melt depletion, and/or end-member starting compositions were somewhat different from those assumed for the figure. In addition, we speculate that the low relative  $^{206}\text{Pb}/^{204}\text{Pb}$  (by  $\sim 0.1$ – $0.2$  for a given  $\epsilon_{\text{Nd}}$  and  $^{87}\text{Sr}/^{86}\text{Sr}$ ) of these lavas compared to the mean data trend might be a consequence of retarded radiogenic Pb growth following the melt-depletion episode(s). Values of  $^{238}\text{U}/^{204}\text{Pb}$  calculated from our U and Pb concentration data for the Cloud cluster are lower by about 16, on average, than values for the E-MORB; if this difference is at least crudely representative of that in the mantle sources, then the “age” of the depletion affecting the sources of the Cloud cluster lavas could be on the order of 40–80 Ma. If so, the Cloud cluster data as a group should tend to lie slightly to the



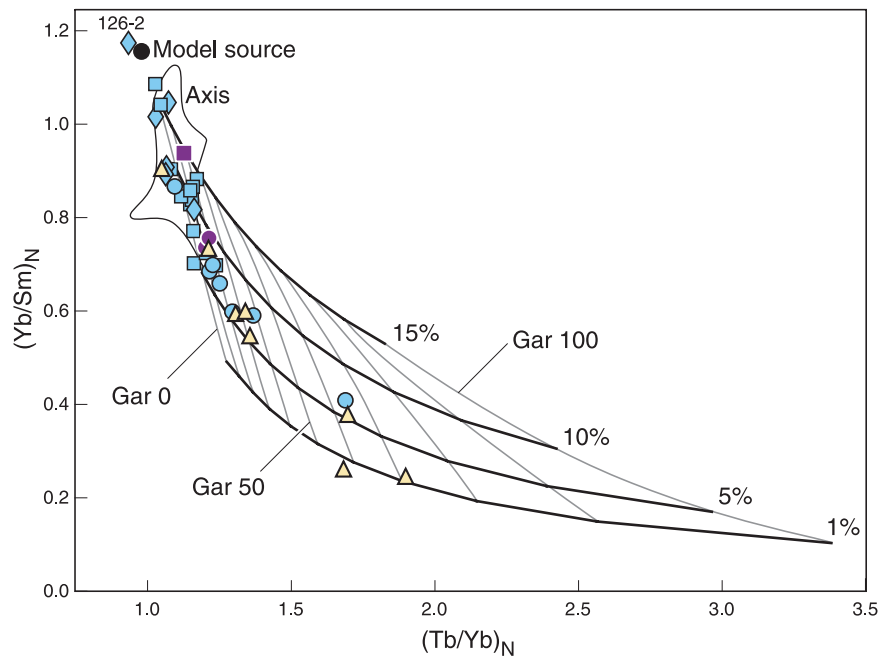


**Figure 14.** Chondrite-normalized  $(\text{Tb}/\text{Yb})_N$  versus  $(\text{Yb}/\text{Sm})_N$ . Symbols are as in Figure 4. The grid indicates the range of model melt compositions produced by 1%, 5%, 10%, and 15% of aggregated fractional melting of peridotite in which the amount of melting that occurs in the presence of garnet varies from 0–100%. The proportion of melt formed in the presence of garnet (Gar) is indicated by light lines; curves of constant melt fraction are shown with heavy lines. The curves are for a source consisting of 75% of estimated average depleted mantle [Workman and Hart, 2005] and 25% of model enriched mantle peridotite [Ito and Mahoney, 2005]. Partition coefficients are taken or interpolated from Salters and Stracke [2004]. The unmelted peridotite is assumed to be 53% olivine, 30% orthopyroxene, 10% clinopyroxene, and 7% garnet or spinel, and melting of these minerals is assumed to occur in proportions of 10%, 10%, 40%, and 40%, respectively, after Janney *et al.* [2000]. Normalizing values are from Sun and McDonough [1989].

high- $^{207}\text{Pb}/^{204}\text{Pb}$  side of the overall data trend in Figure 4b, because  $^{207}\text{Pb}/^{204}\text{Pb}$  changes very little on such timescales. For a 0.1–0.2 change in  $^{206}\text{Pb}/^{204}\text{Pb}$ ,  $^{207}\text{Pb}/^{204}\text{Pb}$  would change by only 0.005–0.010; unfortunately, this is less than the analytical errors on our  $^{207}\text{Pb}/^{204}\text{Pb}$  measurements. Even so, six of the nine Cloud cluster samples do exhibit slightly high  $^{207}\text{Pb}/^{204}\text{Pb}$  relative to their  $^{206}\text{Pb}/^{204}\text{Pb}$  values.

### 6.3. Relationship of Seamounts to Axial Magma Supply and Isotopic Peak

[37] Axial cross section and morphology indicate the entire axis between 16°S and 20°S has an abundant magma supply [e.g., Scheirer and Macdonald, 1993]. The combined data for the seamount field and axial basalts suggest that one reason might be the presence of relatively C-rich mantle, slightly more fusible than ambient mantle to the north and south. However, the distribution of seamounts is poorly related to indicators of axial magma supply. The projected latitudes of most Rano Rahi seamounts are south of 17.5°S, whereas

the most robust axial magma supply is between 16.75°S and 18°S [e.g., Sinton *et al.*, 1991, 2002; Scheirer and Macdonald, 1993; Auzende *et al.*, 1996].

[38] The most strongly C-like isotopic compositions in the entire Rano Rahi field are reached by lavas with projected latitudes of 16–17°S (Figures 9a–9c). Yet at the axis, the highest Pb and Sr and lowest Nd isotope ratios occur at 17–17.5°S. To the east of the axis, our limited sampling on the Nazca plate suggests they may occur even farther south (~17.6–18.1°S). This offset may simply reflect the particular shape of an eastward-flowing C-rich stream or concentration of mantle where it encounters the region of melting. Additionally, although asthenospheric flow beneath the Pacific plate in this region appears likely to be eastward overall, the near-axis asthenosphere may also have a component of southward motion relative to the axis [Mahoney *et al.*, 1994; Kurz *et al.*, 2005].

[39] It seems likely that the northern latitudinal peak in the Pacific-plate Rano Rahi data (Figures 9a–9d) marks a more or less separate stream or

concentration of *C*-rich mantle from that represented by the southern peak, which corresponds to the region where seamounts are most numerous, form the longest chains, and merge with the Pukapuka ridge system. However, the bimodal latitudinal distribution of isotopic values defined by the Pacific-plate Rano Rahi samples contrasts with the single broad isotopic peak along axis. Differences in volume of mantle melted, amount of magma mixing, and average degree of partial melting between Rano Rahi and axial magmas probably account for most of this difference in isotopic patterns. For example, the two latitudinal peaks in the Rano Rahi data are far less apparent when samples with  $(\text{CaO}/\text{Al}_2\text{O}_3)_8 < 0.73$  (i.e., those with values less than on the axis between 16°S and 20.7°S) are excluded from Figure 9.

#### 6.4. Origin of the Seamount Field

[40] One idea to explain near-axis, non-hot spot seamount chains invokes early melting of fertile heterogeneities in the mantle beneath a spreading center [e.g., *Davis and Karsten*, 1986]. Melting farther off axis has been attributed to small-scale mantle convection, lithospheric extension at a high angle to spreading direction, and self-propagating hydrofracture of the lithosphere [e.g., *Winterer and Sandwell*, 1987; *Shen et al.*, 1993; *Sandwell et al.*, 1995; *Scheirer et al.*, 1996a; *Binard et al.*, 1996; *Hieronymus and Bercovici*, 2000]. Recently, fractures resulting from vertical variations in lithospheric cooling rate have been proposed to cause seamount volcanism [*Gans et al.*, 2003; *Sandwell and Fialko*, 2004]. No evidence has been found of fractures along or adjacent to the Rano Rahi chains [*Shen et al.*, 1993], but fractures might be “healed” rather quickly by injections of magma even where seamounts are not generated.

[41] Two features of the Rano Rahi field appear particularly significant: the great majority of seamounts are on the Pacific plate, and a major change appears to have occurred beginning between the time of the last dated Pukapuka ridge volcanism (5.6 Ma) and the oldest dated southern Rano Rahi seamounts (4.4 Ma), which appear to be an outgrowth of the Pukapuka ridge system. In our study area, most of the seamounts are in a wedge-shaped area with projected latitudes south of 17.5°S. This area is more than 200 km wide east of ~115.8°W (Figure 1b) but narrows westward toward the Pukapuka ridge system, characterized by a maximum width of only 70 km. What might be the reason for this change?

[42] *Wessel and Kroenke* [2000] argued that between 5 and 6 Ma, a change in plate motion caused significantly greater N-S tensional stress in Pacific-plate seafloor between 13°S and 23°S, and noted that the Rano Rahi field lies within this region. However, seamount production has been distributed very unevenly. We suggest the concentration of seamounts in the wedge-shaped area east of the Pukapuka ridge system may be the combined result of (a) a persistent stream or concentration of slightly more fusible, *C*-rich asthenosphere flowing from the west, and (b) persistent vulnerability of the lithosphere in this area to N-S tensional stress. By 7.6 Ma, the Pukapuka ridge system had intersected the EPR; subsequent, relatively voluminous Pukapuka ridge volcanism continued near the axis for another ~2 Myr [*Sandwell et al.*, 1995; *Janney et al.*, 2000]. A zone of relatively hot and thin lithosphere may have been formed in the vicinity of the eastern Pukapuka ridge system, extending to the EPR axis. With increasing regional N-S extension, this lithosphere would have been prone to propagation of cracks. Once the process had begun, crack-related seamount volcanism may have tended to maintain itself [*Hieronymus and Bercovici*, 2000]. The lack of a comparable axis-ward widening of the northern seamount chains and the relative paucity in our study area of seamounts with projected latitudes north of 17.5°S suggest to us that *C*-rich mantle streaming from the west reached the axis later at these latitudes and that, overall, the supply of such mantle there has been more fitful than farther south.

[43] Finally, why are seamounts so much less abundant on the Nazca plate? *Wessel and Kroenke* [2000] suggested it is because regional stress conditions are different on this side of the EPR. We suggest that it additionally is a consequence of regional eastward asthenospheric flow [cf. *Davis and Karsten*, 1986]; that is, that the more-fusible *C*-rich material in the mantle flowing from the west is largely (though clearly not completely, as the Nazca-plate seamounts between 17.6°S and 18.1°S show) tapped out by seamount volcanism west of the axis and by axial volcanism, leaving less available for off-axis volcanism east of the axis.

## Appendix A

[44] Representative Rano Rahi seamount samples were analyzed for major element composition both

**Table A1.** Glass Major Element Compositions of Samples Analyzed for Isotopes and Trace Elements<sup>a</sup>

Sample	SiO <sub>2</sub>	TiO <sub>2</sub>	Al <sub>2</sub> O <sub>3</sub>	FeO*	MnO	MgO	CaO	Na <sub>2</sub> O	K <sub>2</sub> O	P <sub>2</sub> O <sub>5</sub>	S	Sum	(CaO/ Al <sub>2</sub> O <sub>3</sub> ) <sub>8</sub>	K <sub>2</sub> O/ TiO <sub>2</sub>	Mg#
66-3	49.65	1.38	16.47	8.88	0.15	7.90	11.67	3.02	0.12	0.15	0.11	99.50	0.71	0.08	61
68-3	47.85	1.15	17.25	11.15	0.19	8.13	11.43	2.81	0.02	0.07	0.12	100.17	0.66	0.02	57
68-4	47.86	1.20	17.33	10.91	0.20	8.26	11.29	2.73	0.01	0.08	0.12	99.99	0.65	0.01	57
70-1	47.94	1.21	17.91	10.22	0.18	8.26	11.17	2.91	0.06	0.11	0.11	100.08	0.62	0.05	59
70-2	48.02	1.16	18.02	9.93	0.18	8.53	11.19	2.86	0.07	0.10	0.11	100.15	0.62	0.06	60
71-1	47.92	1.40	17.33	10.17	0.18	8.93	10.84	2.93	0.05	0.10	0.12	99.97	0.62	0.04	61
72-2	47.84	1.15	17.86	9.94	0.15	8.82	11.21	2.91	0.04	0.09	0.12	100.12	0.63	0.03	61
72-7	47.47	1.08	17.38	11.02	0.15	9.51	10.83	2.63	0.02	0.06	0.11	100.27	0.63	0.02	61
73-4	47.28	1.29	17.91	10.23	0.14	8.41	11.14	3.21	0.02	0.09	0.12	99.84	0.62	0.02	59
76-1	48.40	2.10	16.02	10.24	0.19	7.49	10.58	3.52	0.14	0.25	0.13	99.06	0.67	0.07	57
77-1	49.15	2.07	16.87	8.95	0.19	7.18	10.39	3.60	0.46	0.32	0.11	99.26	0.63	0.22	59
78-1	47.53	1.19	17.58	10.45	0.19	8.78	11.19	2.87	0.05	0.10	0.11	100.04	0.63	0.04	60
78-2	47.24	1.16	17.39	10.13	0.18	9.20	11.20	2.92	0.03	0.08	0.11	99.65	0.65	0.03	62
79-2	47.48	1.10	17.37	10.80	0.18	8.57	11.14	2.86	0.03	0.07	0.12	99.72	0.64	0.03	59
80-1	47.90	1.35	17.85	8.91	0.18	8.52	11.40	3.26	0.03	0.14	0.11	99.64	0.64	0.02	63
81-2a	48.12	1.09	17.68	9.84	0.15	8.32	11.20	2.98	0.04	0.11	0.12	99.64	0.63	0.04	60
82-2	47.85	1.18	17.60	9.28	0.17	9.19	11.31	3.03	0.04	0.10	0.11	99.87	0.65	0.03	64
85-1	48.69	1.52	17.11	9.16	0.16	8.24	11.21	3.09	0.12	0.17	0.11	99.56	0.65	0.08	62
86-1	48.30	1.42	17.69	9.21	0.15	8.04	11.07	3.21	0.11	0.15	0.11	99.46	0.62	0.08	61
89-1	48.82	1.76	16.73	8.89	0.15	7.99	11.17	3.22	0.14	0.21	0.11	99.19	0.67	0.08	62
91-1	49.73	1.26	16.08	9.05	0.16	8.09	12.09	2.78	0.05	0.10	0.12	99.50	0.75	0.04	61
94-2	48.70	1.09	16.26	8.96	0.17	8.64	12.35	2.47	0.06	0.09	0.12	98.90	0.79	0.05	63
94-4	49.25	0.94	16.94	8.68	0.16	9.03	12.86	2.14	0.04	0.07	0.11	100.21	0.82	0.04	65
95-1	48.88	1.14	17.96	8.20	0.14	8.83	11.95	2.86	0.04	0.09	0.11	100.20	0.70	0.03	66
97-2	49.70	1.27	15.69	9.95	0.18	8.24	12.35	2.52	0.05	0.09	0.13	100.17	0.80	0.04	60
98-1	50.19	1.52	14.46	10.94	0.20	7.31	12.20	2.71	0.05	0.11	0.15	99.84	0.83	0.03	54
99-1	49.18	1.43	17.59	8.62	0.16	8.07	11.35	3.56	0.06	0.18	0.12	100.33	0.64	0.04	63
99-3	49.14	1.42	17.69	8.64	0.14	8.16	11.31	3.55	0.05	0.17	0.11	100.39	0.64	0.04	63
100-1	49.05	1.30	17.67	9.10	0.17	7.98	11.43	3.22	0.07	0.14	0.11	100.24	0.65	0.05	61
101-1	48.90	1.98	17.65	8.67	0.17	7.28	10.16	3.78	0.56	0.32	0.11	99.57	0.59	0.28	60
101-7	48.98	2.42	16.92	9.38	0.18	6.38	10.19	3.94	0.50	0.38	0.13	99.40	0.65	0.21	55
102-3	48.75	1.37	17.10	9.03	0.18	8.40	12.16	2.94	0.05	0.10	0.12	100.21	0.72	0.04	62
103-3	49.81	1.40	15.10	10.19	0.18	7.50	12.36	2.90	0.07	0.11	0.13	99.75	0.81	0.05	57
104-1	47.15	0.92	18.08	10.91	0.20	8.70	11.62	2.40	0.03	0.06	0.10	100.17	0.64	0.03	59
104-3	47.14	0.93	17.86	10.92	0.19	9.08	11.47	2.40	0.02	0.08	0.09	100.17	0.64	0.02	60
106-1	49.44	1.19	16.23	9.11	0.17	8.49	12.70	2.52	0.04	0.09	0.13	100.10	0.80	0.03	62
107-1	48.40	1.23	16.92	10.31	0.18	9.07	11.43	2.69	0.08	0.08	0.11	100.49	0.68	0.06	61
108-4	48.09	1.06	18.16	8.37	0.13	9.54	12.06	2.71	0.02	0.06	0.10	100.30	0.77	0.02	67
109-1	49.54	0.87	16.69	8.34	0.14	9.45	12.86	2.03	0.02	0.05	0.11	100.10	0.89	0.03	67
111-6	49.99	1.31	15.98	9.65	0.19	8.13	12.15	2.78	0.06	0.10	0.12	100.47	0.76	0.05	60
112-4	49.58	0.97	16.00	9.53	0.18	8.74	13.02	2.10	0.02	0.06	0.12	100.32	0.85	0.02	62
113-1	47.75	1.11	18.02	9.26	0.16	9.49	11.32	2.86	0.06	0.11	0.11	100.26	0.64	0.06	65
113-2	47.81	1.13	18.19	9.37	0.16	9.18	11.49	2.88	0.06	0.10	0.11	100.47	0.63	0.06	64
114-1	49.67	1.33	15.59	10.14	0.18	7.84	12.40	2.76	0.06	0.08	0.13	100.17	0.79	0.04	58
115-1	49.12	0.96	17.30	9.03	0.15	9.12	12.48	2.35	0.05	0.07	0.11	100.74	0.79	0.05	64
116-1	50.92	1.28	14.49	10.70	0.19	7.61	12.66	2.45	0.05	0.09	0.15	100.59	0.86	0.04	56
117-6	48.72	0.95	17.44	8.81	0.16	9.41	12.49	2.24	0.04	0.07	0.11	100.42	0.82	0.04	66
119-1	47.84	1.14	18.26	8.93	0.16	9.40	11.96	2.53	0.06	0.07	0.11	100.46	0.74	0.05	65
119-3	48.30	1.28	17.51	8.99	0.17	9.53	11.63	2.65	0.09	0.11	0.11	100.37	0.68	0.07	65
119-6	49.87	1.34	16.28	9.00	0.16	8.43	12.34	2.51	0.16	0.13	0.11	100.33	0.77	0.12	63
120-1	50.26	0.97	15.61	9.07	0.17	8.61	13.09	2.19	0.02	0.07	0.12	100.19	0.87	0.02	63
121-2	50.39	1.23	15.79	8.47	0.15	8.28	12.29	2.40	0.13	0.13	0.10	99.38	0.79	0.11	64
122-2	50.04	2.18	14.21	12.05	0.20	7.40	10.62	2.83	0.13	0.22	0.15	100.03	0.74	0.06	52
123-1	50.08	1.83	15.02	10.81	0.20	7.79	11.10	2.68	0.21	0.17	0.14	100.04	0.74	0.12	56
123-2	49.93	2.02	15.56	10.28	0.16	7.30	10.97	2.95	0.30	0.25	0.13	99.86	0.70	0.15	56
124-8	48.70	1.00	17.77	8.86	0.17	9.04	11.95	2.62	0.03	0.06	0.10	100.31	0.72	0.03	65
125-2	49.87	1.71	16.67	8.91	0.17	7.69	11.52	3.18	0.24	0.20	0.11	100.27	0.70	0.14	61
126-2	48.63	0.96	17.36	8.89	0.18	9.43	12.39	2.22	0.03	0.05	0.11	100.24	0.82	0.03	65
127-1	50.05	2.33	14.40	11.76	0.20	6.72	10.44	3.04	0.28	0.25	0.16	99.61	0.74	0.12	50
128-1	49.08	1.61	16.60	9.41	0.19	8.04	11.43	3.10	0.09	0.14	0.11	99.81	0.69	0.06	60
128-3	49.07	2.08	16.00	10.02	0.20	7.09	10.91	3.44	0.19	0.25	0.13	99.37	0.69	0.09	56

**Table A1.** (continued)

Sample	SiO <sub>2</sub>	TiO <sub>2</sub>	Al <sub>2</sub> O <sub>3</sub>	FeO*	MnO	MgO	CaO	Na <sub>2</sub> O	K <sub>2</sub> O	P <sub>2</sub> O <sub>5</sub>	S	Sum	(CaO/ Al <sub>2</sub> O <sub>3</sub> ) <sub>8</sub>	K <sub>2</sub> O/ TiO <sub>2</sub>	Mg#
129-1	50.41	1.73	14.81	10.65	0.19	7.34	11.74	2.70	0.10	0.16	0.14	99.97	0.79	0.06	55
130-3	49.34	2.50	14.16	11.99	0.22	7.44	10.45	2.92	0.15	0.25	0.15	99.57	0.73	0.06	53
130-4	51.07	1.41	15.03	9.24	0.17	7.36	12.36	2.86	0.13	0.12	0.12	99.87	0.81	0.09	59
<b>131-3</b>	48.68	1.85	17.06	8.95	0.19	7.30	11.05	3.42	0.31	0.25	0.11	99.17	0.66	0.17	59
133-3	49.56	1.05	17.07	8.12	0.14	8.84	12.22	2.60	0.04	0.07	0.10	99.82	0.76	0.04	66
<b>134-5</b>	49.25	2.37	15.84	10.09	0.20	6.63	10.55	3.25	0.40	0.36	0.14	99.08	0.68	0.17	54
<b>136-1</b>	50.31	1.98	16.50	9.28	0.15	6.42	9.54	3.47	0.94	0.41	0.11	99.12	0.62	0.48	55
<b>137-1</b>	49.89	1.77	16.31	8.98	0.19	7.41	11.37	3.22	0.17	0.18	0.11	99.59	0.69	0.10	60
<u>137-2</u>	50.70	1.51	15.22	9.54	0.17	7.42	12.15	2.95	0.09	0.13	0.13	100.01	0.79	0.06	58
137-6B	50.62	1.47	15.18	9.43	0.17	7.41	11.99	2.93	0.08	0.12	0.12	99.54	0.78	0.05	58
137-8	50.22	1.32	15.86	8.85	0.18	7.89	12.18	2.81	0.08	0.13	0.12	99.65	0.77	0.06	61
<b>138-1</b>	48.61	3.51	15.98	11.22	0.18	5.04	8.65	3.86	1.19	0.71	0.14	99.10	0.65	0.34	44
<b>138-2</b>	48.54	3.46	15.88	11.03	0.18	5.11	8.57	3.86	1.18	0.72	0.13	98.66	0.65	0.34	45
<b>VG-2</b>															
meas.	50.66	1.86	14.04	11.86	0.21	6.71	11.15	2.66	0.19	0.22	0.15	99.71			
rec.	50.81	1.85	14.06	11.84	0.22	6.71	11.12	2.62	0.19	0.20	0.13	99.86			

<sup>a</sup> Boldface sample numbers indicate E-MORB, defined as having glass K<sub>2</sub>O/TiO<sub>2</sub> ≥ 0.10. Sample numbers in italics indicate the Cloud cluster (see text). Underlined sample numbers indicate samples for which trace element and isotopic analyses were done on rock chips rather than glass. Concentrations are in wt%. FeO\* is total iron as FeO. Measurements were made with a Cameca SX-50 electron microprobe on glass chips; each value is an average of 4–5 measurements from two or more chips (see *Sinton et al.* [1991] for analytical details). Precision (2σ, wt%): SiO<sub>2</sub> 0.65, TiO<sub>2</sub> 0.09, Al<sub>2</sub>O<sub>3</sub> 0.20, FeO\* 0.34, MnO 0.07, MgO 0.14, CaO 0.19, Na<sub>2</sub>O 0.09, K<sub>2</sub>O 0.03, P<sub>2</sub>O<sub>5</sub> 0.04, S 0.01. (CaO/Al<sub>2</sub>O<sub>3</sub>)<sub>8</sub> is calculated from regressions of CaO and Al<sub>2</sub>O<sub>3</sub> versus MgO using Rano Rahi glass-group data combined with glass-group data for the nearby axis (L. S. Hall et al., manuscript in preparation, 2006). Mg# = 100[Mg/(Mg + Fe<sup>2+</sup>)] (atomic), assuming all Fe is in the 2+ oxidation state. Average measured (meas.) values for standard VG-2 (n = 186) analyzed as an unknown during each microprobe session are compared with recommended (rec.) values [Jarosewich et al., 1980].

**Table A2.** Bulk-Rock Major Element Compositions of Samples Analyzed for Isotopes and Trace Elements<sup>a</sup>

Sample	SiO <sub>2</sub>	TiO <sub>2</sub>	Al <sub>2</sub> O <sub>3</sub>	Fe <sub>2</sub> O <sub>3</sub> *	MnO	MgO	CaO	Na <sub>2</sub> O	K <sub>2</sub> O	P <sub>2</sub> O <sub>5</sub>	Sum	K <sub>2</sub> O/ TiO <sub>2</sub>	Mg#
66-3	49.66	1.48	16.58	9.89	0.16	7.85	11.75	2.30	0.23	0.14	100.06	0.16	61
68-3	47.14	1.01	16.85	12.24	0.19	9.15	10.60	2.19	0.21	0.10	99.34	0.20	60
70-2	47.52	1.19	17.82	11.14	0.17	8.80	10.89	2.23	0.10	0.11	100.22	0.08	61
<i>71-1</i>	47.26	1.19	16.75	11.38	0.17	9.35	10.48	2.32	0.24	0.10	99.65	0.20	62
72-2	47.03	1.01	16.90	11.26	0.17	10.84	10.47	2.24	0.04	0.09	99.66	0.04	66
72-7	46.81	0.96	16.43	12.16	0.18	11.71	10.16	2.09	0.01	0.02	99.65	0.01	66
<i>73-4</i>	46.99	1.35	17.03	11.40	0.18	10.21	10.39	2.32	0.08	0.10	99.90	0.06	64
76-1	47.92	1.98	15.99	11.54	0.18	7.22	10.52	2.88	0.21	0.25	99.63	0.11	55
<b>77-1</b>	49.67	2.20	16.90	10.08	0.17	8.01	10.24	2.73	0.56	0.32	101.00	0.26	61
78-2	46.46	1.26	17.07	11.38	0.18	9.33	10.81	2.21	0.05	0.10	99.70	0.04	62
79-2	47.48	1.02	17.40	12.16	0.19	8.99	10.80	2.31	0.04	0.09	99.66	0.04	59
<i>80-1</i>	47.47	1.30	17.81	10.00	0.16	8.36	11.16	2.40	0.12	0.12	99.25	0.09	62
<u>81-2A</u>	46.85	0.96	15.40	11.36	0.17	13.64	9.44	1.93	0.17	0.07	99.89	0.17	70
<u>82-2</u>	46.73	1.16	16.62	10.72	0.17	10.89	10.51	2.18	0.09	0.11	99.69	0.07	67
<u>85-1</u>	47.03	1.67	17.93	10.55	0.16	5.74	11.44	2.50	0.11	0.22	99.65	0.07	52
<u>94-4</u>	48.30	0.91	16.97	9.71	0.15	9.40	12.61	1.65	0.05	0.02	100.07	0.05	66
95-1	47.40	0.91	22.00	7.86	0.13	5.13	12.60	2.33	0.05	0.07	100.19	0.05	56
97-2	48.52	1.28	16.11	11.48	0.18	5.70	12.72	2.22	0.20	0.07	100.28	0.16	50
<u>98-1</u>	49.96	1.46	14.83	12.24	0.20	7.37	12.04	2.28	0.07	0.08	100.28	0.04	54
<u>99-1</u>	48.86	1.36	17.76	9.55	0.16	7.86	11.20	3.11	0.10	0.12	100.19	0.08	62
100-1	47.80	1.26	19.83	10.33	0.14	3.49	12.08	3.10	0.11	0.14	100.22	0.09	40
<b>101-1</b>	48.14	1.90	17.37	9.83	0.16	8.65	9.81	3.60	0.53	0.32	100.34	0.28	64
<b>101-7</b>	47.89	2.15	16.80	10.36	0.18	7.34	9.80	3.27	0.53	0.35	99.84	0.25	58
102-3	47.85	1.23	18.24	9.59	0.16	7.79	11.55	2.98	0.08	0.12	100.53	0.06	62
104-1	46.57	0.87	17.17	12.35	0.20	11.04	10.87	2.25	0.04	0.05	100.94	0.05	64
105-1	48.78	1.09	17.12	9.90	0.18	9.08	12.17	2.50	0.06	0.07	100.71	0.05	64
106-1	48.71	0.96	19.11	8.56	0.14	7.84	13.23	2.19	0.03	0.05	100.45	0.03	64
107-1	47.15	1.12	15.73	11.62	0.18	11.94	10.49	2.41	0.06	0.07	100.00	0.05	67
108-4	47.31	1.05	17.65	9.33	0.15	10.75	11.69	2.55	0.02	0.03	100.22	0.02	70
109-1	49.25	0.85	16.90	9.24	0.15	9.71	12.86	1.90	0.01	0.04	100.46	0.01	68
<u>111-6</u>	49.11	1.27	15.88	10.43	0.18	8.24	12.20	2.64	0.12	0.08	100.20	0.09	61



**Table A2.** (continued)

Sample	SiO <sub>2</sub>	TiO <sub>2</sub>	Al <sub>2</sub> O <sub>3</sub>	Fe <sub>2</sub> O <sub>3</sub> *	MnO	MgO	CaO	Na <sub>2</sub> O	K <sub>2</sub> O	P <sub>2</sub> O <sub>5</sub>	Sum	K <sub>2</sub> O/ TiO <sub>2</sub>	Mg#
112-4	48.99	0.93	15.90	10.24	0.17	8.90	12.93	1.86	0.03	0.03	99.84	0.03	63
113-1	47.26	1.08	17.83	10.11	0.16	10.20	11.19	2.73	0.05	0.07	100.02	0.05	67
114-1	49.30	1.19	16.31	10.71	0.18	8.19	12.20	1.71	0.03	0.06	100.09	0.03	60
115-1	48.07	0.87	17.69	9.55	0.15	9.55	12.16	1.31	0.03	0.04	100.25	0.04	66
116-1	50.81	1.17	14.63	11.36	0.19	7.95	12.60	1.50	0.03	0.07	100.30	0.03	58
117-6	48.34	0.83	18.62	9.01	0.15	9.07	12.63	1.18	0.00	0.04	99.85		67
119-1	47.39	1.02	18.06	9.54	0.16	11.03	11.41	1.44	0.01	0.06	100.10	0.01	70
119-3	48.01	1.23	17.39	9.86	0.16	10.10	11.35	1.69	0.05	0.09	99.91	0.04	67
<b>119-6</b>	49.56	1.22	16.56	9.66	0.16	8.99	12.08	1.51	0.12	0.11	99.95	0.10	65
120-1	50.08	0.90	15.77	9.90	0.17	9.16	12.82	1.23	0.00	0.05	100.06		65
<b>121-2</b>	50.50	1.14	15.99	9.36	0.16	8.79	12.12	1.46	0.07	0.10	99.68	0.06	65
122-2	49.82	2.09	14.10	13.36	0.21	7.58	10.45	1.88	0.11	0.20	99.77	0.05	53
<b>123-1</b>	49.62	1.76	14.87	12.01	0.19	8.00	10.96	1.78	0.17	0.17	99.52	0.10	57
<b>123-2</b>	49.72	1.92	15.31	11.59	0.19	7.69	10.74	1.99	0.30	0.25	99.69	0.16	57
124-8	47.83	0.86	16.57	10.25	0.16	12.17	10.75	1.47	0.00	0.04	100.08		70
<b>125-2</b>	49.36	1.50	16.58	9.72	0.16	8.60	11.24	2.55	0.32	0.20	100.21	0.21	64
126-2	48.33	0.89	17.17	10.15	0.16	10.16	12.09	1.62	0.02	0.05	100.62	0.02	66
<b>127-1</b>	49.55	2.21	14.16	13.42	0.21	7.47	10.20	2.30	0.25	0.24	99.99	0.11	52
128-1	48.53	1.48	15.95	10.69	0.17	9.47	10.89	2.37	0.19	0.14	99.87	0.13	64
129-1	50.20	1.64	14.73	11.66	0.19	7.54	11.69	2.14	0.13	0.14	100.03	0.08	56
130-3	49.38	2.40	21.07	13.65	0.20	7.89	10.42	2.34	0.17	0.25	107.75	0.07	53
130-4	50.85	1.28	15.16	10.18	0.17	8.06	12.12	2.28	0.11	0.11	100.30	0.09	61
133-3	49.63	1.02	16.85	9.28	0.14	9.14	12.12	2.15	0.02	0.07	100.39	0.02	66
<b>134-5</b>	48.86	2.26	16.06	11.16	0.18	6.85	10.48	2.90	0.56	0.31	99.88	0.25	55
<u>137-1</u>	49.57	1.62	17.18	9.94	0.15	7.00	11.76	2.71	0.25	0.20	100.35	0.15	58
<u>137-6</u>	49.93	1.26	17.01	9.82	0.16	7.34	12.37	2.30	0.09	0.11	100.36	0.07	60
137-8	49.45	1.15	18.33	9.36	0.15	7.88	12.13	2.35	0.07	0.10	100.97	0.06	63
<b>138-1</b>	48.19	3.26	16.11	12.67	0.19	6.17	8.44	3.40	1.24	0.69	100.35	0.38	49
<b>BCR-1</b>													
meas.	54.43	2.23	13.56	13.63	0.18	3.49	7.00	3.28	1.71	0.37	99.85		
rec.	54.11	2.24	13.64	13.41	0.18	3.48	6.95	3.27	1.69	0.36	99.33		
<b>BHVO-1</b>													
meas.	49.47	2.78	13.65	12.39	0.16	7.17	11.39	2.20	0.52	0.28	100.00		
rec.	49.94	2.71	13.80	12.23	0.17	7.23	11.40	2.26	0.52	0.27	100.53		

\* Sample numbers in boldface, italics, or underlined as in Table A1. Concentrations are in wt%. Fe<sub>2</sub>O<sub>3</sub>\* is total iron as Fe<sub>2</sub>O<sub>3</sub>. Measurements were made using a Siemens 303-AS XRF spectrometer. Typical absolute uncertainties (2σ, wt%) are SiO<sub>2</sub> 0.2, TiO<sub>2</sub> 0.1, Al<sub>2</sub>O<sub>3</sub> 0.2, Fe<sub>2</sub>O<sub>3</sub> 0.05, MnO 0.01, MgO 0.05, CaO 0.1, Na<sub>2</sub>O 0.1, K<sub>2</sub>O 0.01, P<sub>2</sub>O<sub>5</sub> 0.01. An estimate of accuracy is provided by comparison of measured and recommended [Govindaraju, 1994] values for standards BCR-1 (n = 2) and BHVO-1 (n = 2).

by electron microprobe on glass chips and by XRF on powdered whole rocks. A subset of these analyzed samples was selected for isotopic and/or trace element analysis. Major element compositions for this subset measured by electron microprobe are presented in Table A1, and those measured by XRF are presented in Table A2.

## Acknowledgments

[45] We are indebted to the crew of the R/V *Melville* for making Leg 8 of the Gloria expedition a success. Equally crucial were R. Batiza (co-chief scientist), J. Boaz (Scripps marine tech), K. Johnson, K. Rubin, J. S. Sinton, J. Bailey, A. Cheng, D. Foss, Z. Jurado-Chichay, T. Hulsebosch, P. Johnson, L. Liu (now Ford), R. Nelson, A. Pietruszka, J. Woycke, and G. Yamada. D. VonderHaar, N. Hulbert, and J. Huard helped with various shore-based aspects of the

project. We thank P. Janney, an anonymous reviewer, C. Chauvel, and W. White for comments that significantly improved the manuscript. This work was funded by NSF grants OCE9116266, OCE9811136, and OCE9912379.

## References

- Auzende, J.-M., et al. (1996), Recent tectonic, magmatic, and hydrothermal activity on the East Pacific Rise between 17°S and 19°S: Submersible observations, *J. Geophys. Res.*, *101*, 17,995–18,010.
- Bach, W., E. Hegner, J. Erzinger, and M. Satir (1994), Chemical and isotopic variations along the superfast spreading East Pacific Rise from 6° to 30°S, *Contrib. Mineral. Petrol.*, *116*, 365–380.
- Batiza, R., and D. Vanko (1984), Petrology of young Pacific seamounts, *J. Geophys. Res.*, *89*, 11,235–11,260.
- Binard, N., P. Stoffers, R. Hekinian, and R. C. Searle (1996), Intraplate en-echelon ridges in the South Pacific west of the Easter microplate, *Tectonophysics*, *263*, 23–37.

- Cochran, J. R. (1986), Variations in subsidence rates along intermediate and fast spreading mid-ocean ridges, *Geophys. J. R. Astron. Soc.*, *87*, 421–454.
- Cormier, M.-H., D. S. Scheirer, and K. C. Macdonald (1996), Evolution of the East Pacific Rise at 16°–19°S since 5 Ma: Bisection of overlapping spreading centers by new, rapidly propagating ridge segments, *Mar. Geophys. Res.*, *18*, 53–84.
- Davis, E. E., and J. L. Karsten (1986), On the cause of the asymmetric distribution of seamounts about the Juan de Fuca Ridge: Ridge-crest migration over a heterogeneous asthenosphere, *Earth Planet. Sci. Lett.*, *79*, 385–396.
- Detrick, R. S., A. J. Harding, G. M. Kent, J. A. Orcutt, J. C. Mutter, and P. Buhl (1993), Seismic structure of the southern East Pacific Rise, *Science*, *259*, 499–503.
- Donnelly, K. E., C. H. Langmuir, and S. L. Goldstein (2003), Geochemical constraints on melting processes in the GLIMPSE region, *Eos Trans. AGU*, *84*(46), Fall Meet. Suppl., Abstract V21B-05.
- Duncan, R. A. (2002), A time frame for construction of the Kerguelen Plateau and Broken Ridge, *J. Petrol.*, *43*, 1109–1119.
- Duncan, R. A., and L. G. Hogan (1994), Radiometric dating of young MORB using the <sup>40</sup>Ar–<sup>39</sup>Ar incremental heating method, *Geophys. Res. Lett.*, *21*, 1927–1930.
- Dunn, R. A., and D. W. Forsyth (2003), Imaging the transition between the region of mantle melt generation and the crustal magma chamber beneath the southern East Pacific Rise with short-period Love waves, *J. Geophys. Res.*, *108*(B7), 2352, doi:10.1029/2002JB002217.
- Forsyth, D. W., and GLIMPSE Science Team (2004), On the origin of non-hotspot, intraplate volcanic ridges and gravity lineations, with constraints from the GLIMPSE experiment, *Eos Trans. AGU*, *85*(28), West. Pac. Geophys. Meet. Suppl., Abstract T12A-03.
- Forsyth, D. W., S. C. Webb, L. M. Dorman, and Y. Shen (1998), Phase velocities of Rayleigh waves in the MELT Experiment on the East Pacific Rise, *Science*, *280*, 1235–1238.
- Gans, K. D., D. S. Wilson, and K. C. Macdonald (2003), Pacific Plate gravity lineaments: Diffuse extension or thermal contraction?, *Geochem. Geophys. Geosyst.*, *4*(9), 1074, doi:10.1029/2002GC000465.
- Govindaraju, K. (1994), Compilation of working values and sample description for 383 geostandards, *Geostand. Newsl.*, *18*, spec. issue, 1–158.
- Graham, D. W., A. Zindler, M. D. Kurz, W. J. Jenkins, R. Batiza, and H. Staudigel (1988), He, Pb, Sr and Nd isotope constraints on magma genesis and mantle heterogeneity beneath young Pacific seamounts, *Contrib. Mineral. Petrol.*, *99*, 446–463.
- Hammond, W. C., and D. R. Toomey (2003), Seismic velocity anisotropy and heterogeneity beneath the Mantle Electromagnetic and Tomography Experiment (MELT) region of the East Pacific Rise from analysis of *P* and *S* body waves, *J. Geophys. Res.*, *108*(B4), 2176, doi:10.1029/2002JB001789.
- Hanan, B. B., and D. W. Graham (1996), Lead and helium isotope evidence from oceanic basalts for a common deep source of mantle plumes, *Science*, *272*, 991–995.
- Herzberg, C., P. Rateron, and J. Zhang (2000), New experimental observations on the anhydrous solidus for peridotite KLB-1, *Geochem. Geophys. Geosyst.*, *1*(11), doi:10.1029/2000GC000089.
- Hieronimus, C. F., and D. Bercovici (2000), Non-hotspot formation of volcanic chains: Control of tectonic and flexural stresses on magma transport, *Earth Planet. Sci. Lett.*, *181*, 539–554.
- Ito, G., and J. J. Mahoney (2005), Flow and melting of a heterogeneous mantle: 1. Importance to the geochemistry of ocean island and mid-ocean ridge basalts, *Earth Planet. Sci. Lett.*, *230*, 29–46.
- Janney, P. E., J. D. Macdougall, J. H. Natland, and M. A. Lynch (2000), Geochemical evidence from the Pukapuka volcanic ridge system for a shallow enriched mantle domain beneath the South Pacific superswell, *Earth Planet. Sci. Lett.*, *181*, 47–60.
- Jarosewich, E., J. A. Nelson, and J. A. Norberg (1980), Reference samples for microprobe analysis, *Geostand. Newslett.*, *4*, 43–47.
- Koppers, A. A. P. (2002), ArArCALC—Software for Ar-40/Ar-39 age calculations, *Comput. Geosci.*, *28*, 605–619.
- Kurz, M. D., M. Moreira, J. Curtice, D. E. Lott, III, J. J. Mahoney, and J. M. Sinton (2005), Correlated helium and neon isotopes on the super-fast spreading East Pacific Rise near 17°S, *Earth Planet. Sci. Lett.*, *232*, 125–142.
- Macdougall, J. D., and G. W. Lugmair (1986), Sr and Nd isotopes in basalts from the East Pacific Rise: Significance for mantle heterogeneity, *Earth Planet. Sci. Lett.*, *77*, 273–284.
- Mahoney, J. J., J. M. Sinton, M. D. Kurz, J. D. Macdougall, K. J. Spencer, and G. W. Lugmair (1994), Isotope and trace element characteristics of a superfast spreading ridge: East Pacific Rise, 13–23°S, *Earth Planet. Sci. Lett.*, *121*, 173–193.
- Neal, C. R. (2001), The interior of the Moon: The presence of garnet in the primitive, deep lunar mantle, *J. Geophys. Res.*, *106*, 27,865–27,885.
- Niu, Y.-L., D. G. Wagoner, J. M. Sinton, and J. J. Mahoney (1996), Mantle source heterogeneity and melting processes beneath seafloor spreading centers: East Pacific Rise 18°–19°S, *J. Geophys. Res.*, *101*, 27,711–27,733.
- Niu, Y.-L., M. Regelous, I. J. Wendt, R. Batiza, and M. O'Hara (2002), Geochemistry of near-EPR seamounts: Importance of source vs. process and the origin of enriched mantle component, *Earth Planet. Sci. Lett.*, *199*, 327–345.
- Phipps Morgan, J., W. J. Morgan, Y.-S. Zhang, and W. H. F. Smith (1995), Observational hints for a plume-fed, suboceanic asthenosphere and its role in mantle convection, *J. Geophys. Res.*, *100*, 12,753–12,767.
- Renne, P. R., A. L. Deino, R. C. Walter, B. D. Turrin, C. C. Swisher, T. A. Becker, G. H. Curtis, W. D. Sharp, and A.-R. Jaouni (1994), Intercalibration of astronomical and radioisotopic time, *Geology*, *22*, 783–786.
- Salteras, V. J. M., and A. Stracke (2004), Composition of the depleted mantle, *Geochem. Geophys. Geosyst.*, *5*, Q05B07, doi:10.1029/2003GC000597.
- Sandwell, D., and Y. Fialko (2004), Warping and cracking of the Pacific plate by thermal contraction, *J. Geophys. Res.*, *109*, B10411, doi:10.1029/2004JB003091.
- Sandwell, D. T., E. L. Winterer, J. Mammerickx, R. A. Duncan, M. A. Lynch, D. A. Levitt, and C. L. Johnson (1995), Evidence for diffuse extension of the Pacific plate from Pukapuka ridges and cross-grain gravity lineation, *J. Geophys. Res.*, *100*, 15,087–15,099.
- Scheirer, D. S., and K. C. Macdonald (1993), Variation in cross-sectional area of the axial ridge along the East Pacific Rise: Evidence for the magmatic budget of a fast spreading center, *J. Geophys. Res.*, *98*, 7871–7885.
- Scheirer, D. S., K. C. Macdonald, D. W. Forsyth, and Y. Shen (1996a), Abundant seamounts of the Rano Rahi seamount field near the southern East Pacific Rise, 15° to 19°S, *Mar. Geophys. Res.*, *18*, 13–52.

- Scheirer, D. S., K. C. Macdonald, D. W. Forsyth, S. P. Miller, D. J. Wright, M.-H. Cormier, and C. M. Weiland (1996b), A map series of the Southern East Pacific Rise and its flanks, 15° to 19°S, *Mar. Geophys. Res.*, *18*, 1–12.
- Shaw, D. M. (1970), Trace element fractionation during anatexis, *Geochim. Cosmochim. Acta*, *34*, 237–243.
- Shen, Y., D. W. Forsyth, D. S. Scheirer, and K. C. Macdonald (1993), Two forms of volcanism: Implications for mantle flow and off-axis crustal production on the west flank of the Southern East Pacific Rise, *J. Geophys. Res.*, *98*, 17,875–17,889.
- Sinton, J. M., S. M. Smaglik, J. J. Mahoney, and K. C. Macdonald (1991), Magmatic processes at superfast spreading mid-ocean ridges: Glass compositional variations along the East Pacific Rise 13°–23°S, *J. Geophys. Res.*, *96*, 6133–6155.
- Sinton, J., E. Bergmanis, K. Rubin, R. Batiza, T. K. P. Gregg, K. Grönvold, K. C. Macdonald, and S. M. White (2002), Volcanic eruptions on mid-ocean ridges: New evidence from the superfast spreading East Pacific Rise, 17°–19°S, *J. Geophys. Res.*, *107*(B6), 2115, doi:10.1029/2000JB000090.
- Smith, W. H. F., and D. T. Sandwell (1997), Global seafloor topography from satellite altimetry and ship depth soundings, *Science*, *277*, 1956–1962.
- Sun, S.-S., and W. F. McDonough (1989), Chemical and isotopic systematics of oceanic basalts: Implications for mantle composition and processes, in *Magmatism in the Ocean Basins*, edited by A. D. Saunders and M. J. Norry, *Geol. Soc. Spec. Publ.*, *42*, 313–345.
- Todt, W., R. A. Cliff, A. Hanser, and A. W. Hofmann (1996), Evaluation of a <sup>202</sup>Pb-<sup>205</sup>Pb double spike for high-precision lead isotope analysis, in *Earth Processes: Reading the Isotopic Code*, *Geophys. Monogr. Ser.*, vol. 95, edited by A. Basu and S. Hart, pp. 429–437, AGU, Washington, D. C.
- Wessel, P., and L. W. Kroenke (2000), Ontong Java Plateau and late Neogene changes in Pacific plate motion, *J. Geophys. Res.*, *105*, 28,255–28,277.
- White, W. M., A. W. Hofmann, and H. Puchelt (1987), Isotope geochemistry of Pacific mid-ocean ridge basalt, *J. Geophys. Res.*, *92*, 4881–4893.
- Winterer, E. L., and D. T. Sandwell (1987), Evidence from enechelon cross-grain ridges for tensional cracks in the Pacific plate, *Nature*, *329*, 534–537.
- Workman, R. K., and S. R. Hart (2005), Major and trace element composition of the depleted MORB mantle (DMM), *Earth Planet. Sci. Lett.*, *231*, 53–72.
- Zindler, A., H. Staudigel, and R. Batiza (1984), Isotope and trace element geochemistry of young Pacific seamounts: Implications for the scale of upper mantle heterogeneity, *Earth Planet. Sci. Lett.*, *70*, 175–195.